ACS OMEGA

http://pubs.acs.org/journal/acsodf

Article

Research on the Law of Head Loss of Jet Pumps in the Cavitation State

Jian Gan, Yanan Wang, Deming Wang,* and Kang Zhang

Cite This: *ACS Omega* 2022, 7, 12661−12679

Read Online

ACCESS | Metrics & More | Article Recommendations

ABSTRACT: Liquid flow is subject to head loss because of viscous force, surface tension, friction force, and so on. Part of the energy is irreversibly converted into heat, which then dissipates into the environment. Head loss intensifies in the turbulent state. At present, few studies explore the law of head loss caused by secondary flow, cavitation intensity, and turbulence intensity. In this study, the head losses in different sections of a jet pump were studied by controlling the cavitation number σ, the secondary flow rate Q_s, and the inlet pressure p_i. The experimental results were analyzed with the aid of computational fluid dynamics. The results show that an increase in Q_s can weaken the variations of Q_s and suction pressure p_s in the transitional stage of cavitation. Besides, σ, Q_s, and p_i influence head loss to varying extents. Cavitation intensity and turbulence intensity are the main factors for head loss and jet temperature difference. In particular, the influence of Q_s on head loss provides guidance both for reducing the energy loss of the quantitative adding device and jet aerator and for expanding the stable adding range of the jet. More importantly, the main factors of energy loss caused by jet cavitation were analyzed in detail, which can effectively facilitate the pipeline design to reduce the local and frictional head loss.

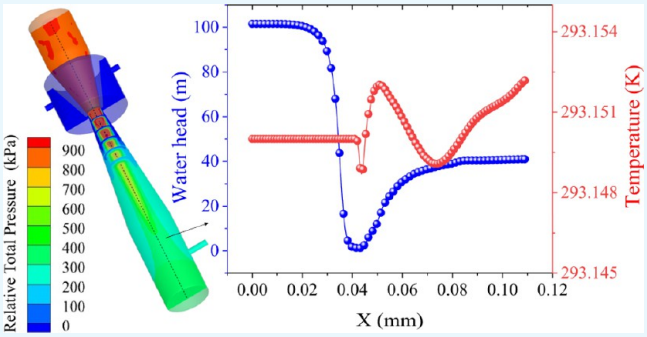

1. INTRODUCTION

Jet pumps have long been used for the purposes of aeration, pumping, and evaporation. They are applied in the fields of chemical industries, environmental treatment, civil engineering, agriculture, mining, and mechanical engineering,[1−6] including water treatment, refrigeration, desalination, mixing, and dredging.[7] The most important concern in these fields is the pressure drop (energy loss) of the jet pump, which generally attracts attention in the above fields and is directly related to the determination of power equipment capacity, the working range of quantitative water addition, and the energy consumption in water treatment.

Zhu et al. designed nine kinds of jet pumps with different area ratios via the combination of three nozzles and four diffusion pipes and proposed empirical curves to optimize the area ratio on the basis of given flow ratios. They concluded that with respect to a given optimal area ratio, when the critical flow ratio was smaller than 1.4%, the critical pressure ratio was larger than 0.8.[8] Lu and Long studied cavitating jet pumps[9] and found that when the critical pressure ratio h_{cr} was smaller than 0.4, the operating range was small and the driving ability was weak. Gao proposed a parameter estimation method based on head loss adjustment to estimate the pipeline roughness of the water supply network. The experimental results proved the effectiveness of this method in estimating pipeline roughness.[10] Yang and Cao reported the effects of head loss, surface tension, viscosity, and density on the Kelvin−Helmholtz instability (KHI) of two typical pipelines (i.e., a straight pipeline with different cross-sections and a bend pipeline). They also investigated the law of normal water head loss in straight pipelines and bend pipelines.[11] Chen et al. put forward a multi-evel evaluation method for Venturi tube corrosion, which realized the accurate correction of the pressure difference of Venturi tubes in the nuclear power plant and served as a reliable reference for improving the safety in operating nuclear power units.[12] Jiang and Gong analyzed the influence of the number, position, and angle of the deflector on the water head loss of a square pipe with a 90° bend through numerical simulation and optimized the deflector installation.[13] Wang et al. used a new adding method of a two-stage cavitation jet, which effectively reduced the pressure loss of the jet pump and improved the stability of surfactants with quantitative addition. This research did not analyze the reasons and laws of reducing pressure loss. Royne[14] and Brignoni[15] analyzed the nozzle

Received: December 6, 2021
Accepted: March 25, 2022
Published: April 6, 2022

https://doi.org/10.1021/acsomega.1c06895
ACS Omega 2022, 7, 12661−12679

pressure drop caused by water and air through different nozzles, respectively, and found that nozzle diameter, length, and chamfer angle were crucial factors for nozzle pressure drop. McNeil[16] disclosed the influence of air with different viscosities and liquids on the nozzle pressure drop. In the hope of improving the performance of jet pumps, researchers have done extensive work from the perspectives of decreasing the pressure drop, analyzing the structure, and optimizing the evaluation methods such as aeration and mixing.

The application of jet pumps is mainly based on its cavitation of the high pressure ratio. However, cavitation is accompanied by the formation, growth, and collapse of bubbles, which releases a large amount of energy. Therefore, it is difficult to obtain a high pressure ratio in the cavitation state. This paper reported an experimental study to investigate the energy loss law of a high-pressure-ratio jet pump without a throat designed according to the recommendations of Zhu and Wang (2018). This study aims to explore the influence law of the cavitation number σ, the secondary flow Q_s, and the inlet pressure p_i on the energy loss in the jet zone (a−b), the mixing zone (b−c), and the diffusion zone (c−d) through quantitative analysis. The research results can provide the guidance and reference for the optimization, design, and application of the jet device in engineering practice.

2. EXPERIMENTAL RIG AND OPERATION PROCESS

2.1. Components of the Experimental System. The experimental system is mainly composed of a jet pump, a storage tank, a plunger pump, a frequency conversion controller, flow meters, valves, a clean water bucket, pressure sensors, and a paperless recorder (Figure 1). The nozzle of the jet pump is made of iron, and the cavitation cavity and diffusion section are made of organic glass. The connecting pipelines in the system adopt high-pressure hoses with an inner diameter of 19 mm and a pressure resistance level of 10 MPa. The pipeline connection is sealed by U-shaped bolts, O-shaped rings, and raw material tapes. Before the experiment, a system sealing experiment was performed. The pressure sensors and flow meters are connected to the paperless recorder through two-core communication cables and connected to the computer through an RS485-USB interface. Before the experiment, the whole system is debugged, and the data monitoring state is checked to ensure normal operation (Table 1).

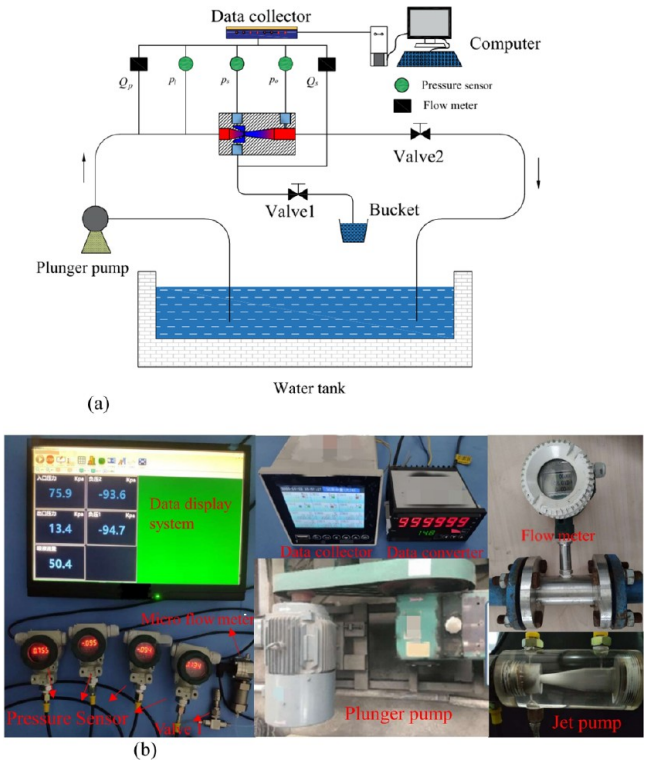

Figure 1. Experimental system. (a) Schematic diagram of the experimental system. (b) Main equipment of the experimental system.

Table 1. Parameters of the Experimental Measuring Instruments

apparatus	model	test range	precision (%)
data collector	BK-0896K		
flow meter 1 (Q_p)	LD-15	0.2−6 m^3/h	0.50
micro flow meter (Q_s)	CX-M5.1	1−1000 mL/min	0.30
pressure sensor 1 (p_i)	BK-23XIM14	0−2.5 MPa	0.30
pressure sensor 2 (p_o)	BK-23XIM14	0−2.5 MPa	0.30
pressure sensor 3 (p_s)	BK-23XIM14	−0.1 to 0.3 MPa	0.30

To obtain a higher critical pressure ratio h_{cr}, a jet pump without a throat was designed and manufactured with reference to Zhu, Lu, and Wang.[4,8,9,17,18] The internal structure and related parameters are given in Figure 2.

2.2. Operation Process. First, the external water supply valve was opened to provide sufficient water in the water tank, the water temperature being 20 ± 2 °C. The outlet valve was fully opened; then, the plunger pump was turned on to operate at a low pressure for a certain time to drain air from the system. After the preparation work, the inlet pressure was set to the predetermined value through the pump inverter. After the inlet pressure stabilized, the cavitation state of the jet pump was changed by the outlet valve. During the experiment, the real-time data were monitored all the time to ensure data reliability.

3. NUMERICAL SIMULATION AND THEORETICAL ANALYSIS

3.1. Numerical Simulation. To explain the experimental results, the characteristics of cavitation, turbulence intensity, and temperature distribution in the jet pump were analyzed with the aid of ANSYS Fluent 2019 R3. Since the numerical simulation adopts transient calculation, the numerical calculation results vary at all times. To solve this problem, the calculation results were recorded every 50 time steps; the data record period is much shorter than the oscillation frequency of the cavitation clouds. Since the cavitation state is the main research object, the results with the widest coverage range of the vapor volume fraction in the convergence results of the transient calculation serve as the calculation basis.

3.1.1. Fluid Domain and Meshing. Figure 3 gives the fluid domain of the jet pump. The origin of the coordinate system is set at the center of cross-section a−a. The directions of the primary and secondary flows are the positive directions of the *X*-axis and *Y*-axis, respectively.

Compared with tetrahedral meshes, hexahedral meshes are dominated by polyhedrons (P-H) and are more adaptable to complex models, thus being able to better capture the details of turbulence. The mesh orthogonal quality of most areas is

https://doi.org/10.1021/acsomega.1c06895
ACS Omega 2022, 7, 12661−12679

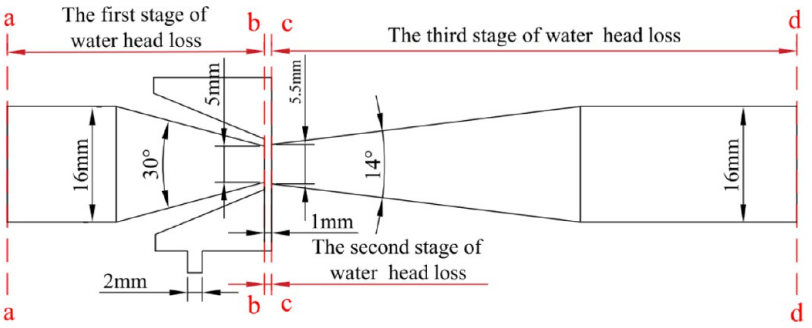

Figure 2. Schematic diagram of the internal structure of the cavitation jet device. (The positions of different cross-sections of the jet pump are marked by a−d.)

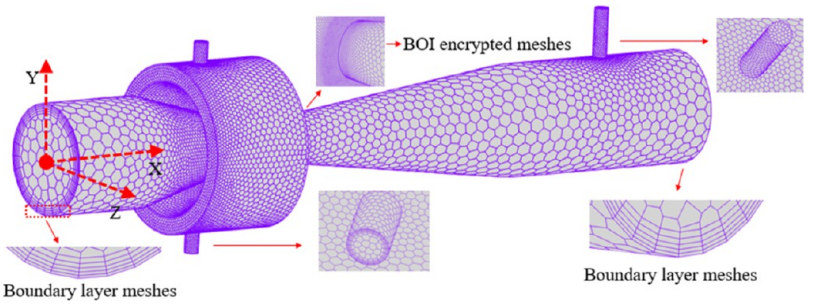

Figure 3. Overall mesh and details.

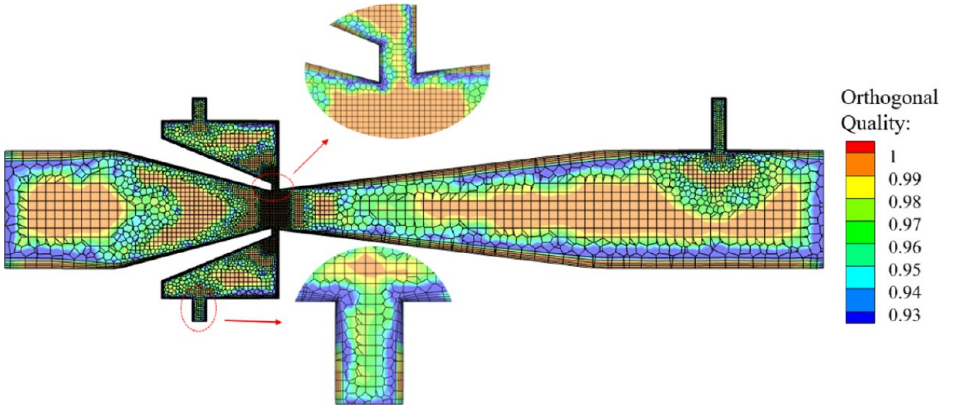

Figure 4. Orthogonal quality of the meshes.

greater than 0.9 (Figure 4). Therefore, the fluid domain of the jet pump was divided into P-H. The unstructured meshes were generated using Fluent Meshing. In the process of mesh generation, the mixing zone (b−c) and the suction tube were encrypted using the unique BOI function of Fluent Meshing. Meanwhile, five layers of boundary meshes were divided to capture the details of fluid flow near the wall. The boundary layer meshes were modified according to the y^+ value range of the wall function. Moreover, mesh independence has been explored. The exploration results suggest that mesh independence can be achieved at about 100,000 mesh elements. The total number of mesh elements in the fluid domain for numerical calculation was 304,089.

3.1.2. Boundary Conditions. The inlet and outlet of the primary liquid served as the pressure boundaries; the secondary flow inlet served as the mass flow boundary. The primary inlet pressure p_i was set to 700, 900, and 1100 kPa, respectively. The mass flow of the secondary flow Q_s was set to 0, 8.1 12.7, and 16.3 L/h, respectively, equivalent to the open degree of valve 1 in Figure 1. A series of simulation calculations were conducted under different outlet pressures p_o.

3.1.3. Description of the Computational Fluid Dynamics Approach. In this study, discretization was conducted using the pressure−velocity coupling method,[19,20] the multiphase flow and turbulent flow were simulated using the mixture model and the realizable k−e turbulence model.[19−21] Besides, the realizable k−e turbulence model was complemented with scalable wall functions. Table 2 shows the selection of discrete schemes of the control equation. The iteration time step was set to 1×10^{-5} s, and the residual error limit of the monitored parameters was 1×10^{-6}. When all the key parameters correspond to residual errors of below 1×10^{-6}, the monitored data become independent of the increase of iteration times. Then, the results are regarded to be convergent.

The wall function is a supplement to the realizable k−e turbulence model. The selection of the standard wall function requires the first mesh nod to be in the turbulent core area, that is, $300 > y^+ > 30$.[22] According to the previous practice,

https://doi.org/10.1021/acsomega.1c06895
ACS Omega 2022, 7, 12661−12679

Table 2. Discrete Schemes of the Control Equation

solution methods	spatial discretization
gradient	least-squares cell-based
pressure	presto
momentum	second-order upwind
volume fraction	quick
turbulent kinetic energy	second-order upwind
turbulent dissipation rate	second-order upwind
energy	second-order upwind

when $400 > y^+ > 11.5$,[23] a higher numerical accuracy can be obtained. Selecting an appropriate y^+ can ensure a higher calculation accuracy and effectively reduce the number of boundary layer meshes. To make the model more suitable for the turbulent environment of high-pressure gradient flow, separated flow, and strong rotating flow, y^+ was modified. According to the model and experimental parameters, L = 0.005, v = 39.49, ρ = 998.2 kg/m^3, and μ = 0.001. Assuming y^+ = 45, R_e = 197,095 and Δs = 0.000024 m. The diameter-changing section of the diffusion tube in the jet pump is where strong turbulence occurs, which deserves more attention. The thickness of the first boundary layer meshes were divided according to Δs. The correction process for the value of y^+ is illustrated in Figure 5.

To better match the realizable k−e turbulent model, scalable wall functions, which can be combined with the standard wall method to achieve the use of the log law, were selected for the near-wall treatment. When $y^+ < 15$, scalable wall functions[23] can avoid the deterioration of the calculation results and give a consistent solution to arbitrarily refined meshes. When the mesh is coarsened and $y^+ > 11$, the performance of scalable wall functions is consistent with that of the standard wall function. Moreover, for arbitrarily refined meshes, scalable wall functions can give a consistent solution.

3.2. Theoretical Analysis. *3.2.1. Cavitation Number.* The cavitation intensity of the jet pump can be expressed by the cavitation number σ[24]

$$\sigma = \frac{p_o - p_v}{\frac{1}{2}p_l v_l^2 p_o} \quad (1)$$

where p_o is the outlet pressure of the jet pump; p_v is the saturated steam pressure of water at the ambient temperature; and v_l is the fluid velocity. The critical cavitation state can reduce the cavitation number of the noncavitation state to the critical cavitation number σ_{cr} by reducing the pressure or increasing the velocity. When $\sigma > \sigma_{cr}$, the jet pump is in a normal working state; when $\sigma < \sigma_{cr}$, the jet pump enters the cavitation state. With the decrease in the value of σ, the cavitation intensity increases and the cavitation becomes increasingly intense.

3.2.2. Critical Pressure Ratio. The working condition of the jet pump is closely related to the pressure ratio h, which is defined as the ratio of the outlet absolute pressure to the inlet absolute pressure of the device. The critical pressure ratio h_{cr} is the critical point between the normal working state and the cavitation state of the jet pump,[18,24,25] which can be expressed as

$$h_{cr} = \left(\frac{p_{o,abs}}{p_{i,abs}}\right)_{cr} \quad (2)$$

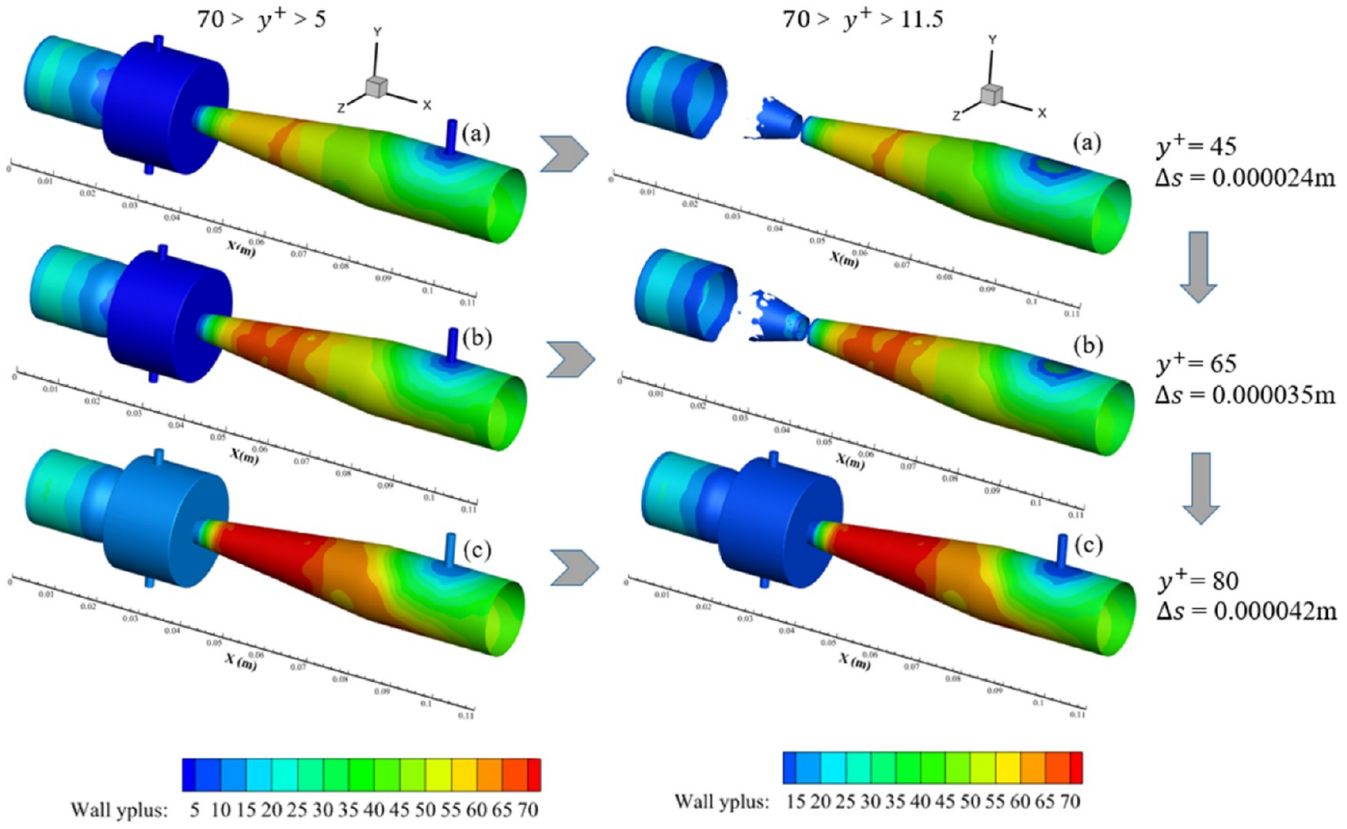

Figure 5. Correction process of the value of y^+. Applicability of the boundary layer meshes when y^+ = 45 (a), y^+ = 65 (b), and y^+ = 80 (c).

https://doi.org/10.1021/acsomega.1c06895
ACS Omega 2022, 7, 12661−12679

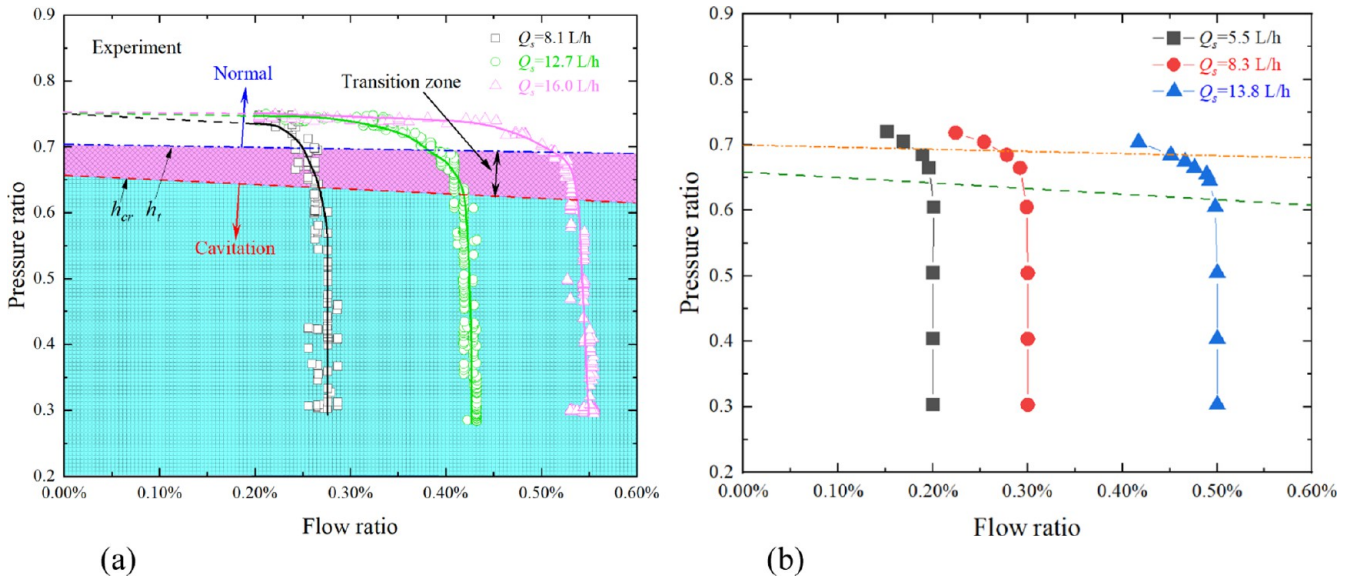

Figure 6. Relationship between h and q_r. (a) Analysis on the experimental results. (b) Analysis on the numerical results.

where $p_{i,abs}$ and $p_{o,abs}$ are the absolute pressures at the inlet and outlet, respectively, and subscripts cr and abs represent the critical point and absolute pressure value, respectively. The critical pressure ratio h_{cr} remains unchanged under the same flow ratio.

3.2.3. Head Loss. The jet pump was divided into three parts to analyze the law of head loss (Figure 2). All the pressures and velocities were taken as area-weighted averages. According to Bernoulli's equation, the local head loss between cross-sections a−a and b−b is

$$H_{a-b} = z_a + \frac{p_a}{\rho_a g} + \frac{\alpha_1 v_a^2}{2g} - z_b - \frac{p_b}{\rho_b g} - \frac{\alpha_2 v_b^2}{2g} \tag{3}$$

where α_1, α_2, z_a, z_b, p_a, p_b, v_a, and v_b are the kinetic energy correction coefficients, water heads of location, average static pressures, and velocities of cross-sections a−a and b−b, respectively. The average elevation of the model cross-section can be regarded as of the same height, that is, $z_a = z_b$. Therefore, eq 3 can be simplified as

$$H_{a-b} = \frac{p_a}{\rho_a g} + \frac{\alpha_1 v_a^2}{2g} - \frac{p_b}{\rho_b g} - \frac{\alpha_2 v_b^2}{2g} \tag{4}$$

The formula of the Reynolds number is

$$R_e = \frac{\rho v L}{\mu} \tag{5}$$

and the formula of turbulence intensity is

$$I = 0.16 R_e^{-1/8} \tag{6}$$

where ρ, μ, v, and L are the density of fluid, dynamic viscosity coefficient, characteristic velocity, and characteristic length of the flow field, respectively. Under a large Reynolds number, the velocity is uniformly distributed, and it can be approximately set to 1. The flow state of the Reynolds number in this study is turbulent. Hence, $\alpha_1 = \alpha_2 = 1$. Equation 4 can be further simplified into

$$H_{a-b} = \frac{p_a}{\rho_a g} + \frac{v_a^2}{2g} - \frac{p_b}{\rho_b g} - \frac{v_b^2}{2g} \tag{7}$$

The b−c head loss H_{b-c} is

$$H_{b-c} = \frac{p_b}{\rho_b g} + \frac{v_b^2}{2g} - \frac{p_c}{\rho_c g} - \frac{v_c^2}{2g} \tag{8}$$

where p_b, p_c, v_b, v_c, ρ_b, and ρ_c are the average static pressures, velocities, and densities of cross-sections b−b and c−c, respectively.

The c−d head loss H_{c-d} is

$$H_{c-d} = \frac{p_c}{\rho_c g} + \frac{v_c^2}{2g} - \frac{p_d}{\rho_d g} - \frac{v_d^2}{2g} \tag{9}$$

The total head loss of the jet pump H_{a-d} is

$$H_{a-d} = H_{a-b} + H_{b-c} + H_{c-d} = \frac{p_a}{\rho_a g} + \frac{v_a^2}{2g} - \frac{p_d}{\rho_d g} - \frac{v_d^2}{2g} \tag{10}$$

The water head at the primary flow inlet is

$$H_{a-a} = \frac{p_a}{\rho_a g} + \frac{v_a^2}{2g} \tag{11}$$

Similarly, it can be deduced that the heads of cross-sections b−b, c−c, and d−d are

$$H_{b-b} = \frac{p_b}{\rho_b g} + \frac{v_b^2}{2g} \tag{12}$$

$$H_{c-c} = \frac{p_c}{\rho_c g} + \frac{v_c^2}{2g} \tag{13}$$

$$H_{d-d} = \frac{p_d}{\rho_d g} + \frac{v_d^2}{2g} \tag{14}$$

Since the head loss values are small, to amplify the difference in head loss, pressure loss instead of head loss was analyzed. The relationship between pressure loss P and water head H is

$$P = \rho g H \tag{15}$$

https://doi.org/10.1021/acsomega.1c06895
ACS Omega 2022, 7, 12661−12679

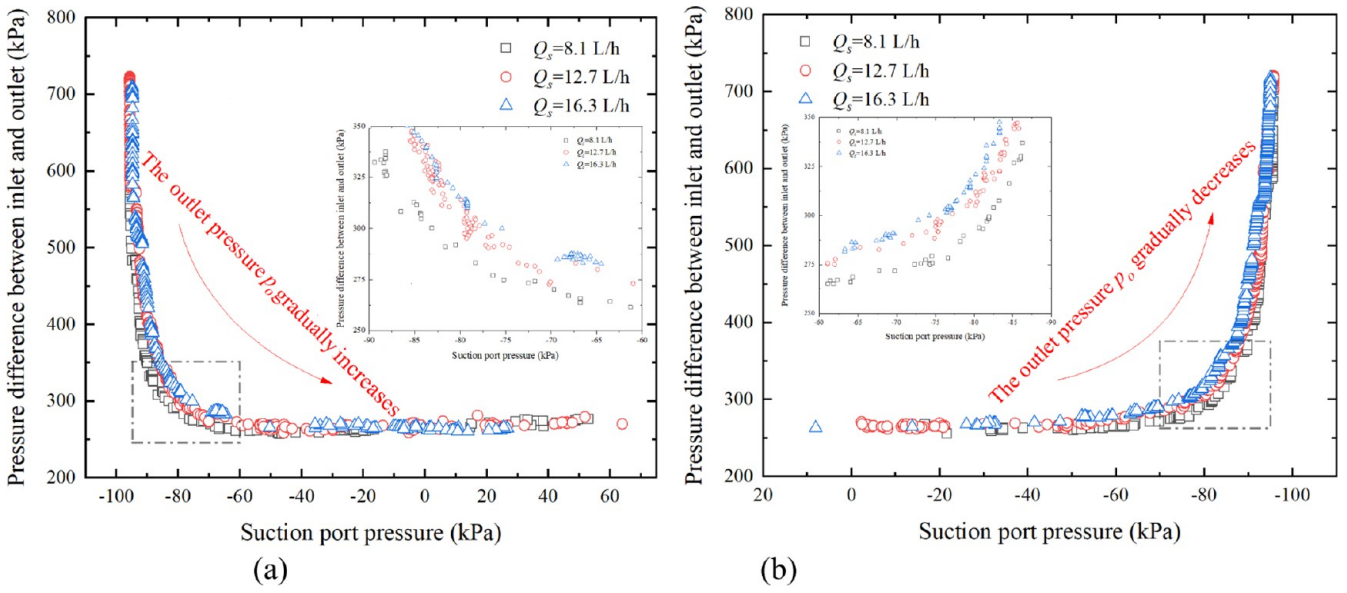

Figure 7. Variation of the pressure difference between the outlet and the inlet of the jet pump with p_s. (a) Process of increasing p_o. (b) Process of reducing p_o.

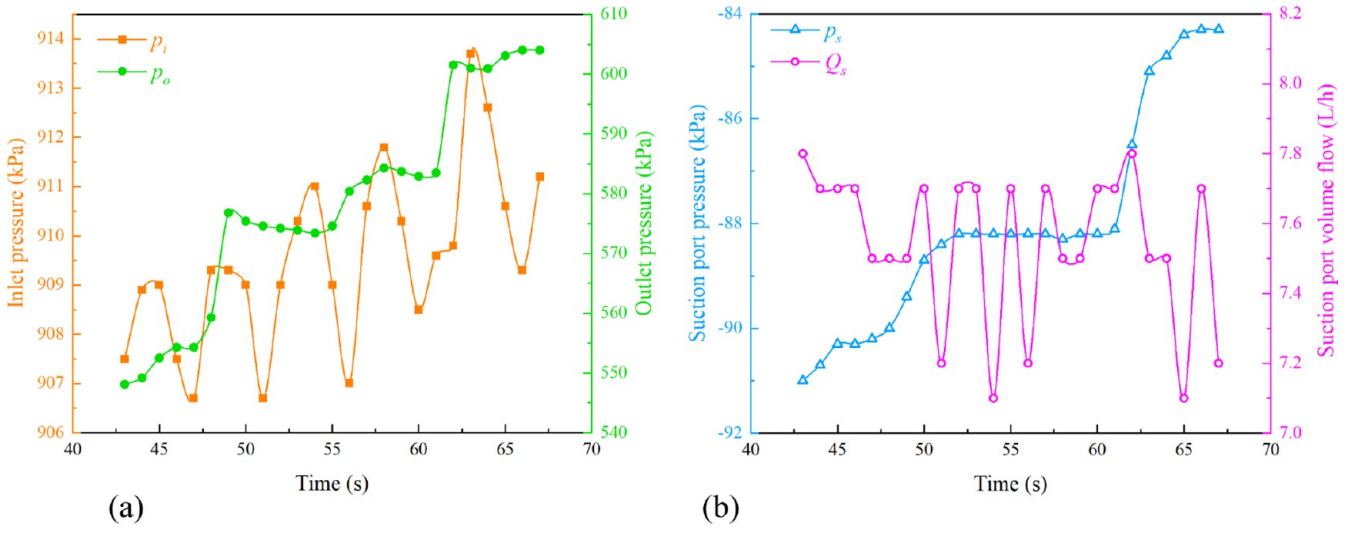

Figure 8. Variations of p_i, p_s, and Q_s when p_i = 900 kPa and q_r = 2.6‰ in the transitional stage. (a) Variation of p_i with p_o. (b) Variations of p_s and Q_s with p_o.

3.2.4. Q-Criterion. The Q-criterion is an important calculation method for vortex identification.[26,27] It can be expressed as

$$Q = 0.5(\|\Omega\|_F^2 - \|S\|_F^2) \tag{16}$$

where $\|\Omega\|_F^2$ is the square of the norm of matrix Ω and matrices Ω and S are the symmetric and antisymmetric tensors of the velocity gradient, respectively

$$\Omega = 0.5[\nabla v\text{-}(\nabla v)^T] \tag{17}$$

$$S = 0.5[\nabla v\text{-}(\nabla v)^T] \tag{18}$$

where ∇v is the velocity tensor and T is the transpose symbol of the matrix. The norms for the tensors are the Frobenius norms, that is, the square root of the sum of the squares of all tensor elements

$$\nabla v = \begin{pmatrix} U_x & U_y & U_z \\ V_x & V_y & V_z \\ W_x & W_y & W_z \end{pmatrix} \tag{19}$$

where U, V, and W are the velocities in the three directions of x, y, and z, respectively. The Q-criterion, which boasts an absolute magnitude to identify vortices, is sensitive to the threshold. Different thresholds in the Q-criterion lead to different visualization results.[25] Generally, an iso-surface with $Q > 0$ is selected as the vortex.

4. RESULTS AND DISCUSSION

4.1. Variations of the Jet Pump Pressure Ratio *h* with the Flow Ratio q_r. Considering the stable and accurate addition function of the jet pump, lower flow ratios were selected for the experiment (q_r = 2.6, 3.3, and 5.3‰). As

https://doi.org/10.1021/acsomega.1c06895
ACS Omega 2022, 7, 12661−12679

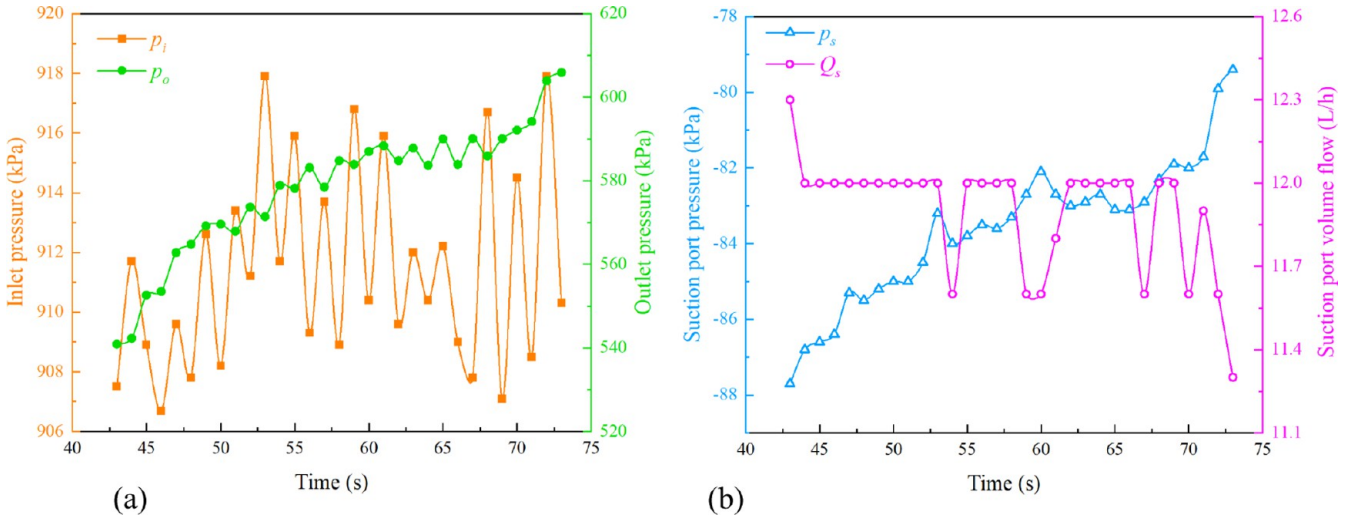

Figure 9. Variations of p_i, p_s, and Q_s when p_i = 900 kPa and q_r = 3.3‰ in the transitional stage. (a) Variation of p_i with p_o. (b) Variations of p_s and Q_s with p_o.

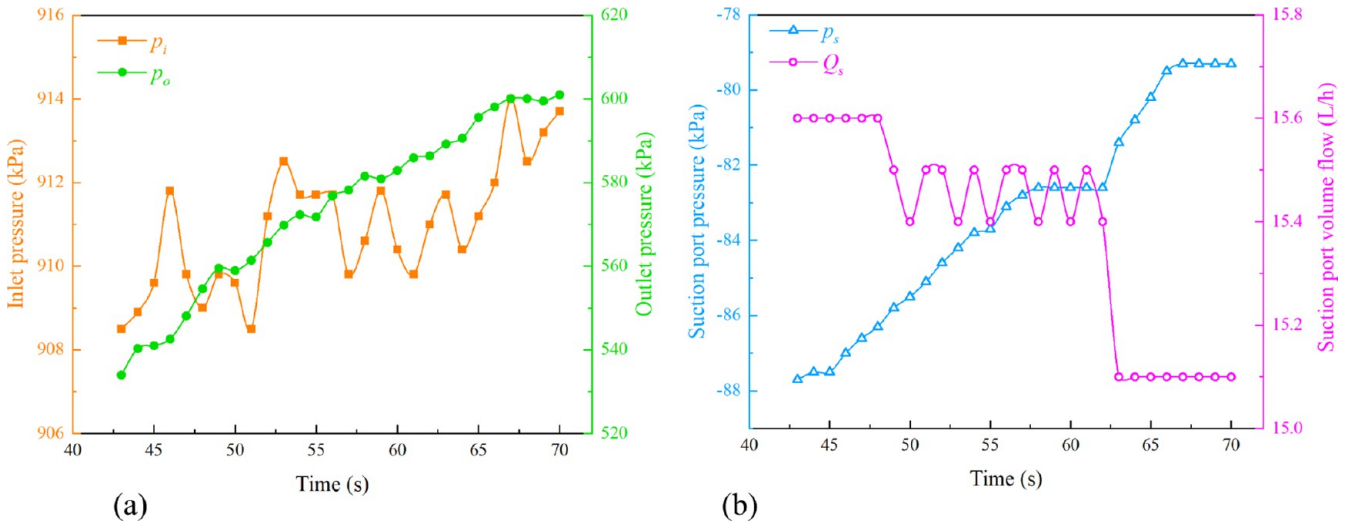

Figure 10. Variations of p_i, p_s, and Q_s when p_i = 900 kPa and q_r = 5.3‰ in the transitional stage. (a) Variation of p_i with p_o. (b) Variations of p_s and Q_s with p_o.

shown in Figure 6, the critical pressure ratio increases with the increase in Q_s. According to the three-colored area in Figure 6a, as the pressure ratio increases, the variation of the flow ratio q_r falls into three stages. When the pressure ratio h is smaller than the critical pressure ratio h_{cr}, the flow ratio remains constant. At this time, the downstream of the nozzle outlet reaches the saturated vapor pressure of water, which causes flow blockage, and the flow ratio does not vary with the pressure ratio. When $h_{cr} < h < h_t$, it belongs to a transitional state of critical cavitation, and the flow ratio gradually decreases as the pressure ratio increases, which is a gradual process (the pink area). When the pressure ratio h is greater than the transitional pressure ratio h_t, cavitation disappears, and the jet pump is in a normal state. As the pressure ratio increases further, the three dashed lines in Figure 6 converge on the Y-axis (the solid lines indicate the measured values, while the dashed lines are the expected values). This convergence is the critical pressure ratio when the secondary flow rate Q_s = 0. The variation of the pressure ratio h directly reflects the static pressure loss of the jet pump. The critical pressure ratio is the critical value between cavitation and the normal working state of the jet pump, which corresponds to the minimum static pressure loss under the cavitation state. The suction flow rate corresponds to the critical pressure ratio. Hence, the accuracy of the simulation was verified by controlling the secondary flow. As displayed in Figure 6b, the simulation results are in good consistency with the experimental results, which indicates the reliability of the numerical calculation in analyzing the pressure loss of the jet pump.

As shown in Figure 7, when the jet pump is in the cavitation state, p_s is between −95 and −100 kPa. The pressure difference range is 500−725 kPa under different suction flow rates. As the suction negative pressure increases, the jet pump enters the transitional stage. At this time, the pressure differences corresponding to different suction flow rates begin to vary. Under the same pressure difference value, the higher the suction flow rate Q_s is, the lower the suction negative pressure is. This is because part of the negative cavitation pressure is transformed into the dynamic pressure of the secondary flow.

https://doi.org/10.1021/acsomega.1c06895
ACS Omega 2022, 7, 12661−12679

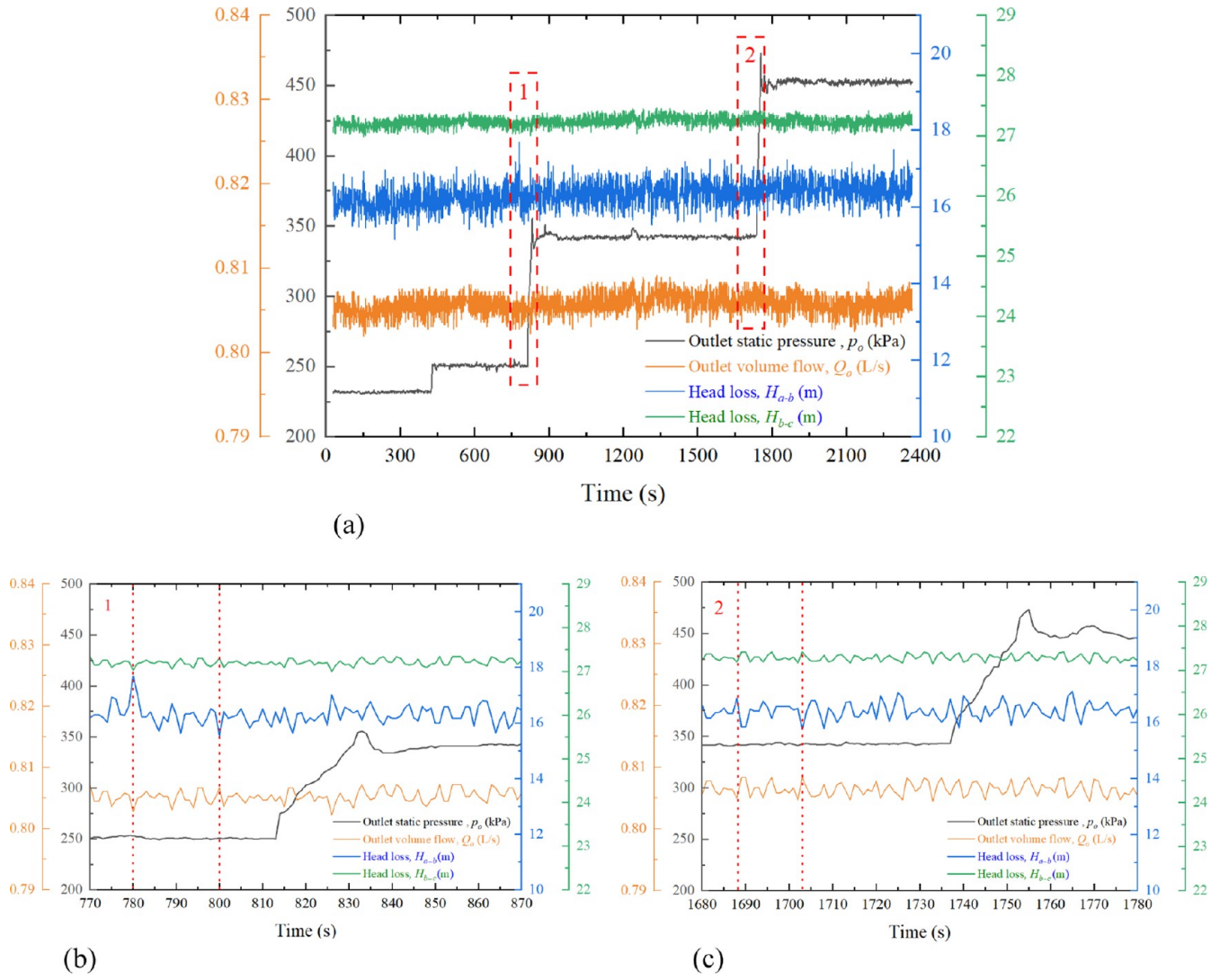

Figure 11. Variations of Q_o, p_o, H_{a-b}, and H_{b-c} when p_i = 900 kPa and Q_s = 0. (a) Variations of Q_o, H_{a-b}, and H_{b-c} with p_o. (b) Enlarged view of area 1 in (a). (c) Enlarged view of area 2 in (a).

The higher the suction flow rate is, the more the cavitation negative pressure is consumed. As the outlet pressure continues to increase, the negative pressure state at the suction port becomes positive. The pressure difference is kept at 265 kPa. Figure 7b shows the process of reducing the outlet pressure. This process is the opposite to the adjustment process in Figure 7a, and they share the same variation.

By adjusting the outlet pressure p_o, the jet pump is changed from the cavitation state to the normal operation state. To facilitate comparison, the data-collecting time is assumed to be in the range of 40−75 s, which does not affect data analysis. As shown in Figures 8−10, the inlet pressure p_i starts to fluctuate and increase as the outlet pressure p_o increases. The sensitivity of the inlet pressure p_i to the variation of the outlet pressure p_o intensifies as the flow ratio q_r increases. During this process, the negative pressure value of the liquid suction port p_s increases slowly, and the suction flow rate of the suction port Q_s decreases gradually. As the outlet pressure increases, the suction flow rate fluctuates steadily for a while. The fluctuation range narrows with the increase in the suction flow rate. When the outlet pressure increases, the negative pressure of the suction port p_s also has a phased stable state. However, the inlet pressure increases with unsteady fluctuations. This shows that when the jet pump is in the transitional stage, a larger secondary flow rate corresponds to a better buffer effect against the outlet pressure variation. This buffering performance is demonstrated by the variations of the secondary flow and suction negative pressure.

4.2. Law of Head Loss of the Jet Pump. When p_i = 900 kPa and Q_s = 0, the outlet pressure p_o is increases gradually by adjusting the outlet valve. In the whole process, the jet pump is in the cavitation state. As shown in Figure 11, the variation of the outlet pressure p_o exerts a limited influence on Q_o, H_{a-b}, and H_{b-c}. However, the outlet flow rate Q_o and H_{a-b} fluctuate. As shown by the dashed lines in Figure 11b,c, when the primary flow is at its peak, H_{b-c} is at the peak and H_{a-b} reaches its lowest value and vice versa. Moreover, this effect is of instantaneity, indicating that Q_o is negatively correlated with H_{b-c} and positively correlated with H_{a-b}. Figure 11 also shows that the oscillation amplitude of H_{a-b} is larger than that of H_{b-c}.

Figure 12 shows the same experimental process in Figure 11. With reference to Figure 12, p_o is negatively correlated with H_{c-d}, yet Q_o is positively correlated with H_{c-d} (the red dashed

https://doi.org/10.1021/acsomega.1c06895
ACS Omega 2022, 7, 12661−12679

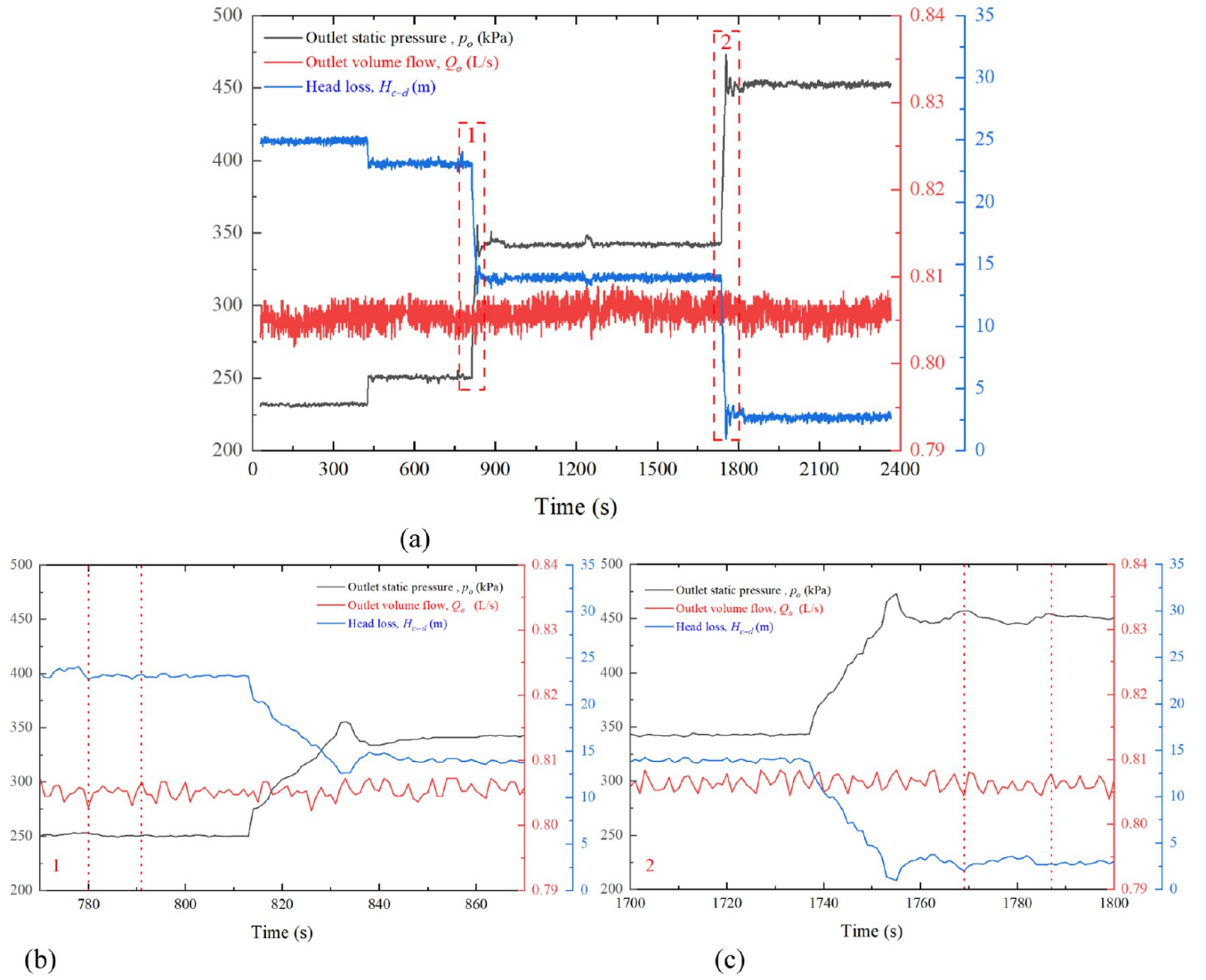

Figure 12. Variations of Q_o, p_o, and H_{c-d} when p_i = 900 kPa and Q_s = 0. (a) Variations of Q_o, p_o, and H_{c-d}. (b) Enlarged view of area 1 in (a). (c) Enlarged view of area 2 in (a).

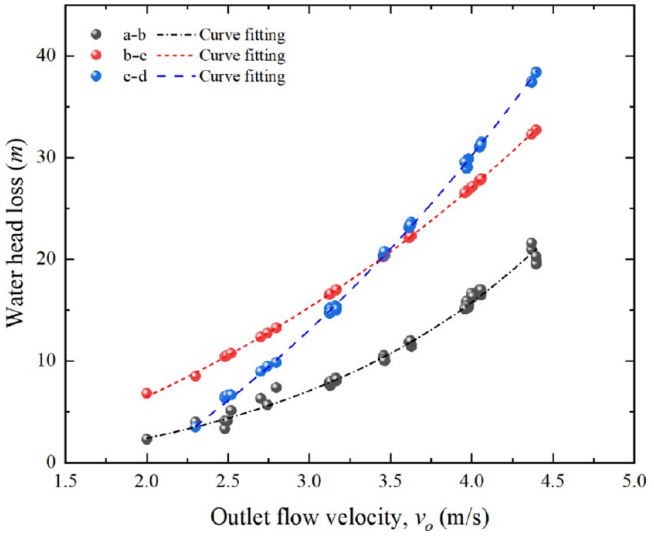

Figure 13. Variation of jet pump head loss with the outlet flow velocity v_o when Q_s = 0.

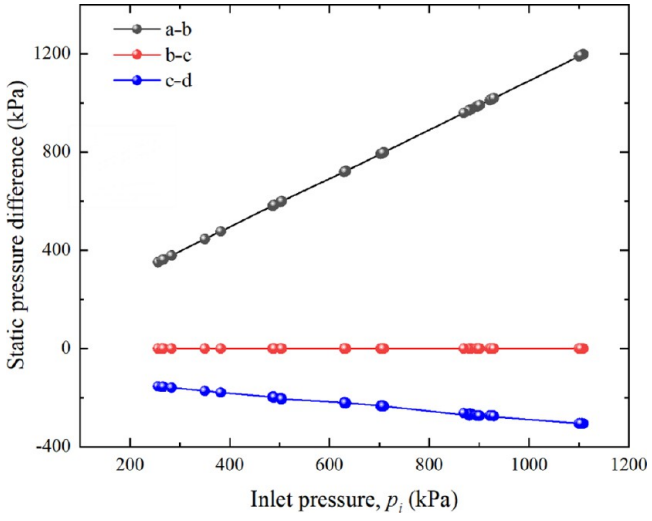

Figure 14. Variation of the static pressure difference with the inlet pressure p_i when Q_s = 0.

https://doi.org/10.1021/acsomega.1c06895
ACS Omega 2022, 7, 12661−12679

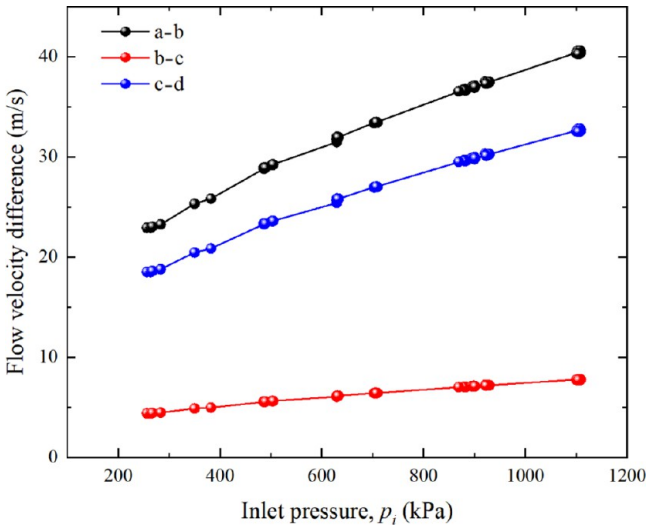

Figure 15. Variation of the flow rate difference with the inlet pressure p_i when Q_s = 0.

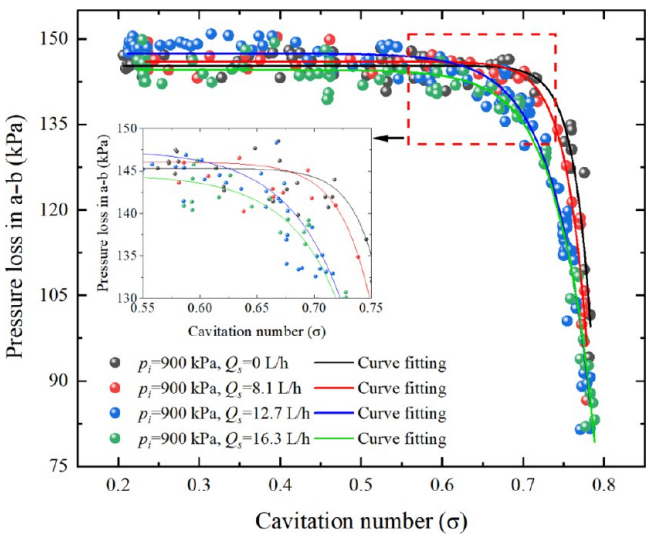

Figure 16. Variation of H_{a-b} with σ.

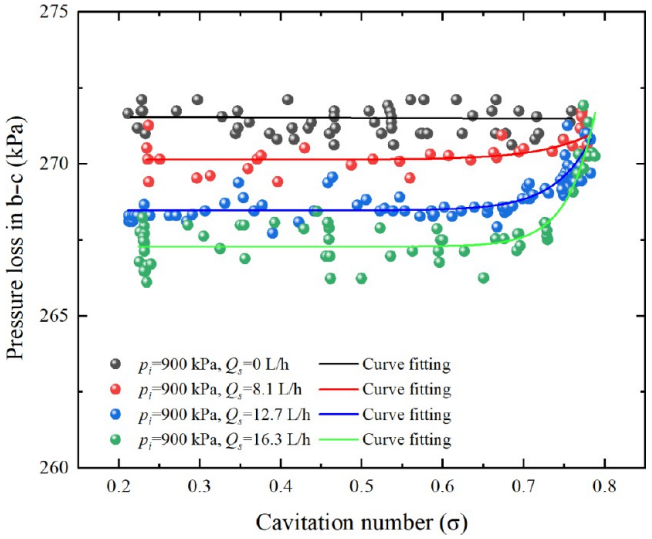

Figure 17. Variation of H_{b-c} with σ.

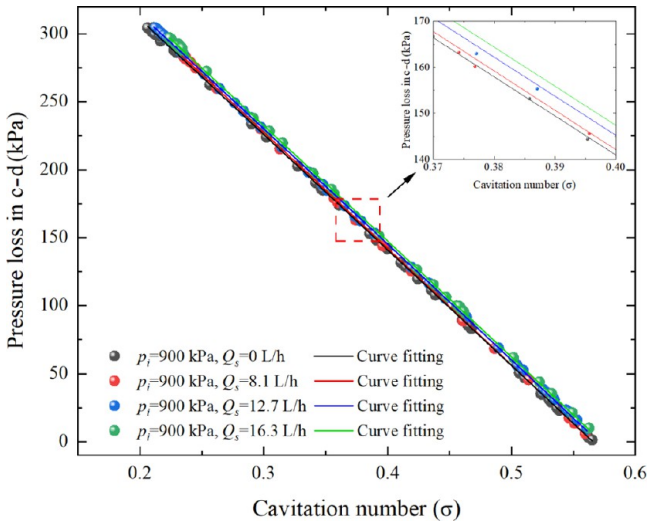

Figure 18. Variation of H_{c-d} with σ.

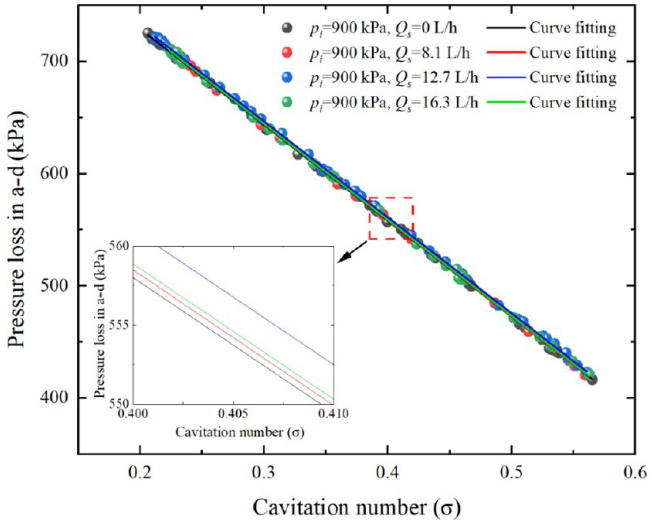

Figure 19. Variation of H_{a-d} with σ.

line in Figure 12). In the cavitation state, the static pressure and dynamic pressure of cross-section c−c as well as the dynamic pressure of cross-section d−d remain constant. However, the static pressure of cross-section d−d increases, so H_{c-d} decreases. this shows that an increase in p_o weakens the turbulence intensity and the cavitation intensity of cross-section c−d, which is reflected in the increase in the static pressure of cross-section d−d. Under the cavitation condition ($\sigma < \sigma_{cr}$), H_{a-b} and H_{b-c} are free from p_o, so H_{c-d} determines H_{a-d}. This conclusion is consistent with the results in Figure 11. The above analysis indicates that the cavitation intensity and turbulence intensity of the diffuser in the cavitation state play a decisive role in H_{c-d} and H_{a-d}.

The outlet valve was fully opened while valve 1 was closed; then, the plunger pump inverter was adjusted so that the inlet pressure of the jet pump was 700, 900, and 1100 kPa, respectively. During this process, the outlet flow rate Q_o is equal to the primary flow rate Q_p. According to Figure 13, H_{a-b}, H_{b-c}, and H_{c-d} increase with the increase in the outlet flow rate. H_{c-d} is more sensitive to the variation of outlet velocity than H_{a-b} and H_{b-c}. When the outlet flow Q_o < 3.5 m/s, H_{b-c} is the largest among the three parts of the jet pump.

https://doi.org/10.1021/acsomega.1c06895
ACS Omega 2022, 7, 12661−12679

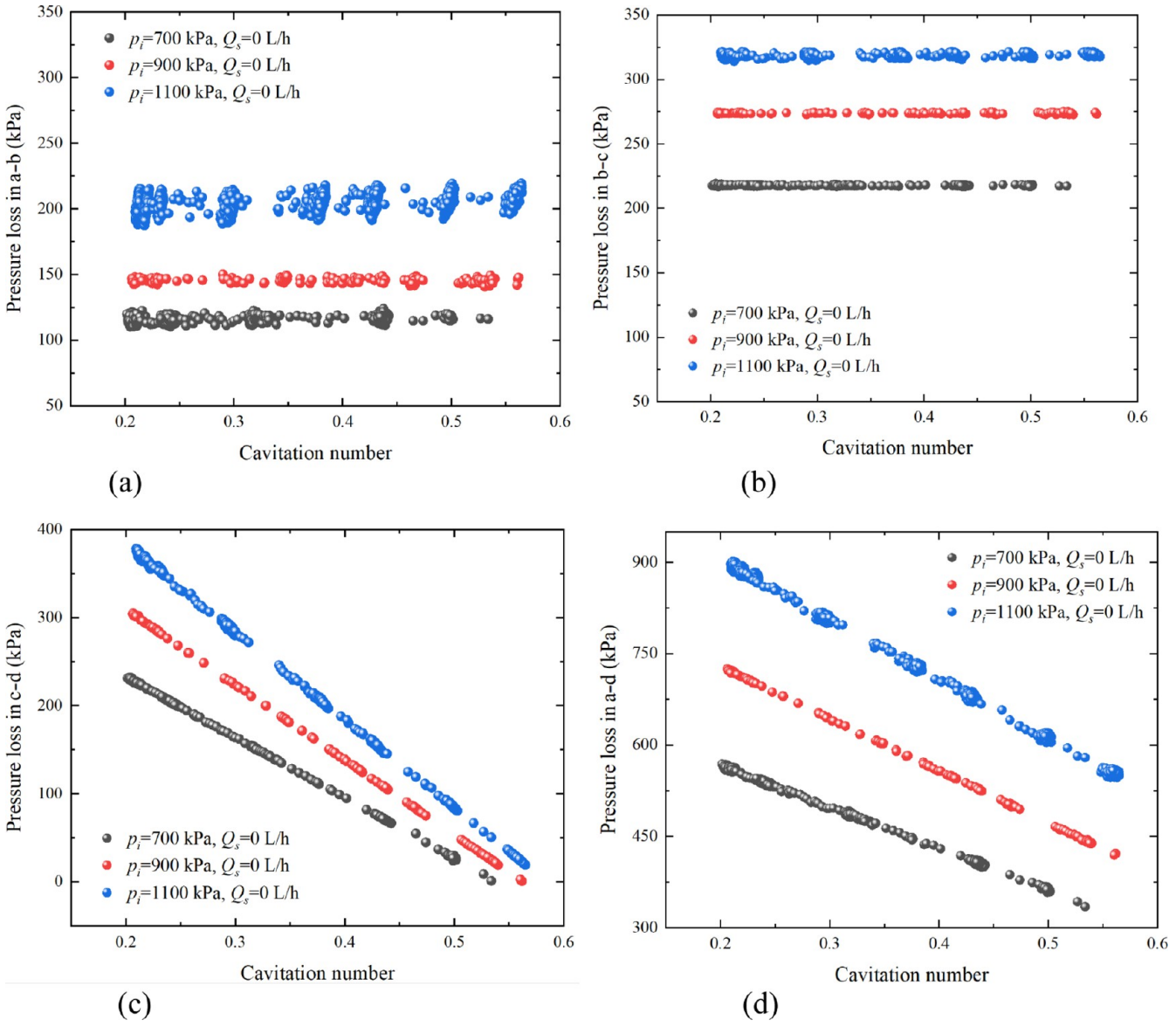

Figure 20. Variation of the pressure loss in different parts of the jet pump with σ when $Q_s = 0$. (a) Variation of H_{a-b} with σ. (b) Variation of H_{b-c} with σ. (c) Variation of H_{c-d} with σ. (d) Variation of H_{a-d} with σ.

When the outlet flow rate $Q_o > 3.5$ m/s, H_{c-d} exceeds H_{b-c} and becomes the largest. This shows that the increase in the primary flow rate plays a significant role in the enhancement of cavitation intensity and turbulence intensity of the diffuser, which leads to an increase in H_{c-d}.

As shown in Figure 14, the a–b static pressure difference is linearly and positively correlated with the inlet pressure p_i; the c–d static pressure difference is negatively correlated with the inlet pressure p_i; however, the b–c static pressure difference remains almost constant. Under the same inlet pressure p_i, the a–b static pressure loss is the largest; the b–c static pressure loss is almost negligible; yet the c–d static pressure is increasing. As the inlet pressure increases, the static pressure increase is smaller than the static pressure loss in cross-section a–b. As displayed in Figure 15, the flow velocity differences in cross-sections a–b, b–c, and c–d are linearly positively correlated with the inlet pressure p_i. Under a constant inlet pressure p_i, cross-sections a–b and b–c correspond to the largest and smallest dynamic pressure loss, respectively. The pressure difference law in Figure 15 is closely related to the abrupt structure change of the flow passage cross-section in the jet pump. It serves as a reference for pipeline design.

4.3. Effect of the Cavitation Number on Pressure Loss. When $p_i = 900$ kPa and $\sigma < 0.6$, the jet pump is in a strong cavitation state with respect to different suction flow rates Q_s. In this state, the pressure difference between cross-sections a–a and b–b remains unchanged. As shown in the fitting curves in Figure 16 (fitted with exponential ExpGrow 1), the pressure loss in cross-section a–b differs slightly at different suction flow rates Q_s. When $Q_s = 12.7$ L/h, the a–b pressure loss is the largest; when $Q_s = 16.3$ L/h, the a–b pressure loss is the smallest. This is caused by the error of the negative pressure at the suction port. Therefore, the pressure loss law of different suction flow rates differs slightly from the predicted situations.

When $p_i = 900$ kPa and $0.75 > \sigma > 0.6$, the jet pump enters the transitional stage of cavitation. The cavitation intensity begins to decrease; the negative pressure area shrinks; and the

https://doi.org/10.1021/acsomega.1c06895
ACS Omega 2022, 7, 12661−12679

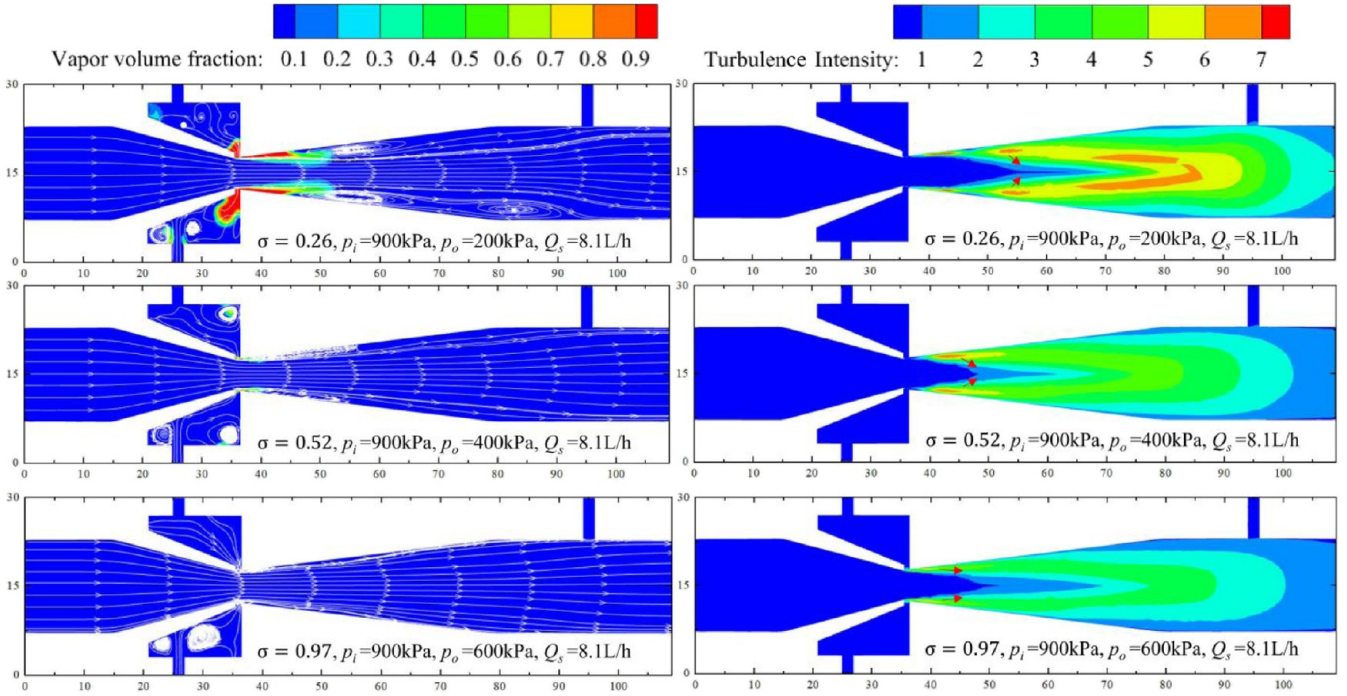

Figure 21. Distribution of vapor volume fraction and turbulence intensity in the cross-section when Z = 0 mm for different cavitation numbers σ.

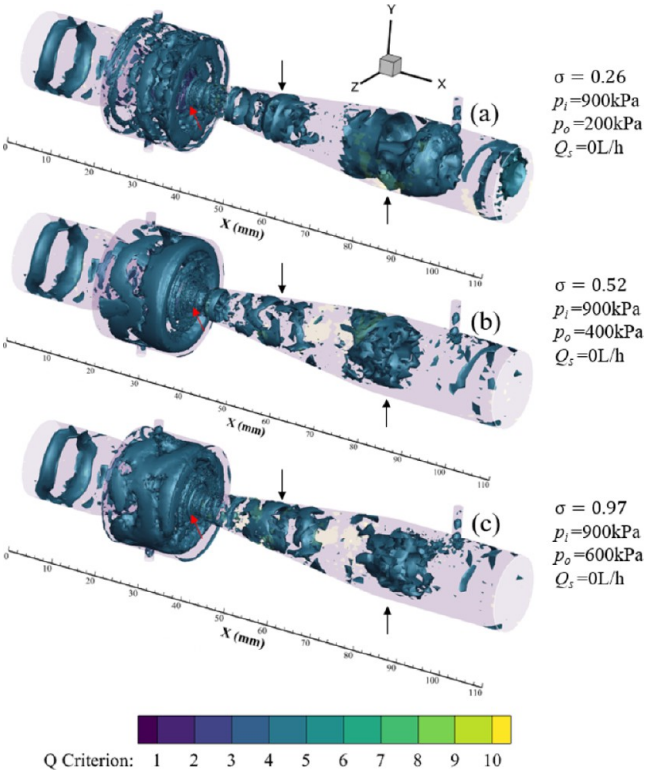

Figure 22. Variation of vortices with σ when Q_s = 0 L/h.

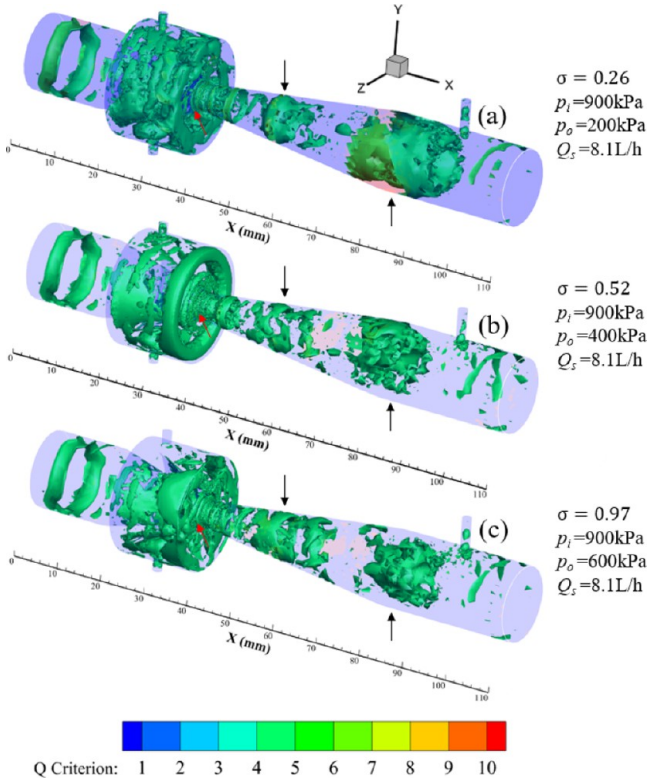

Figure 23. Variation of vortices with σ when Q_s = 8.1 L/h.

suction flow rate Q_s also decreases. The static pressure difference between cross-sections a−a and b−b decreases, while the dynamic pressure remains constant; therefore, the pressure loss in cross-section a−b begins to decrease. When σ > 0.75, the cavitation intensity falls to an extremely small value until the cavitation disappears. At this time, the jet pump enters the normal working state. A further increase in the cavitation number σ leads to a decrease in the primary flow rate, which explains the fast decrease in the a−b pressure loss.

It should be noted that the inflection point, where the pressure loss starts to decrease, differs greatly under different suction flow rates Q_s. Since a high suction flow rate requires a strong cavitation intensity, it is more sensitive to the outlet pressure variation than a small suction flow rate. Therefore, the

https://doi.org/10.1021/acsomega.1c06895
ACS Omega 2022, 7, 12661−12679

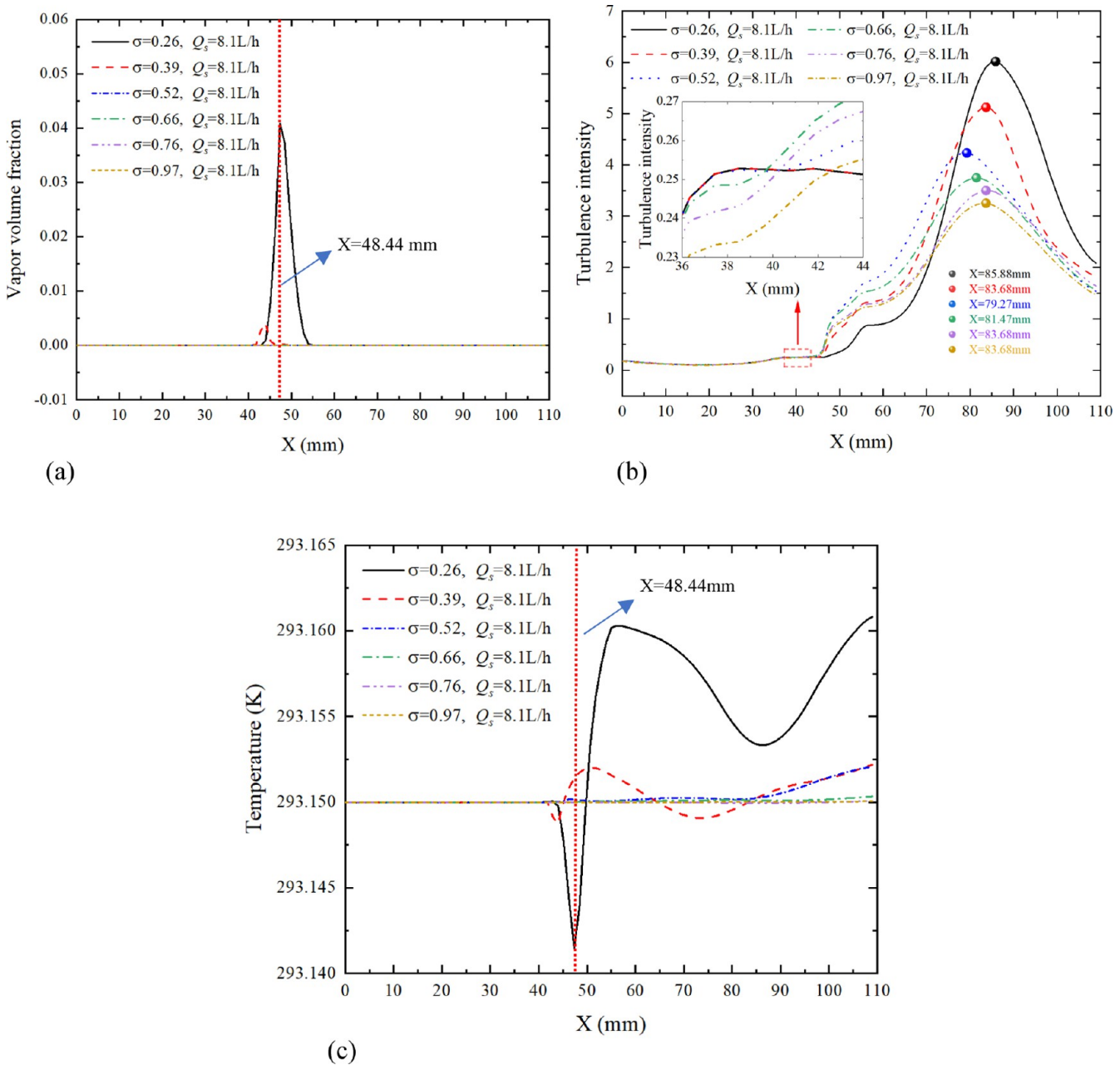

Figure 24. Distribution of vapor volume fraction, turbulence intensity, and temperature on the *X*-axis for different cavitation numbers σ. (a) Vapor volume fraction distribution on the *X*-axis. (b) Turbulence intensity distribution on the *X*-axis. (c) Temperature distribution on the *X*-axis (Figure 3).

inflection point for the pressure loss of the high suction flow rate appears earlier than the low suction flow rate. This is consistent with the law of the critical pressure inflection point.

As shown in Figure 17, when $\sigma < 0.6$, the b−c pressure loss decreases with the increase in the suction flow rate Q_s. An increase in the secondary flow rate Q_s reduces the dynamic pressure difference between cross-sections c−c and b−b. This is consistent with the conclusion in Section 4.2. When $\sigma < 0.6$ and the suction flow rate is constant, the pressure loss in cross-section b−c remains unchanged. When $\sigma > 0.6$, the jet pump changes from the transitional stage to the normal working state, during which the suction flow rate decreases, and the dynamic pressure difference between cross-sections c−c and b−b increases, so the cross-section b−c pressure loss begins to increase.

As shown in Figure 18, for a constant suction flow rate Q_s, the c−d pressure loss decreases linearly with the increase in the cavitation number. This shows that when the dynamic pressure difference between cross-sections c−c and b−b is constant, the cavitation intensity determines the cross-section c−d pressure loss. According to eq 1, when the primary flow and the secondary flow are constant, the c−d cavitation intensity is determined by the outlet pressure of the jet pump. As shown in the fitted curve in Figure 9, for a constant cavitation number σ, the c−d pressure loss increases with the increase in the secondary flow rate.

According to Figure 19, for a constant suction flow rate Q_s, the a−d pressure loss decreases linearly with the increase in the cavitation number σ. With respect to a constant cavitation number σ, the a−d pressure loss increases with the increase in

https://doi.org/10.1021/acsomega.1c06895
ACS Omega 2022, 7, 12661−12679

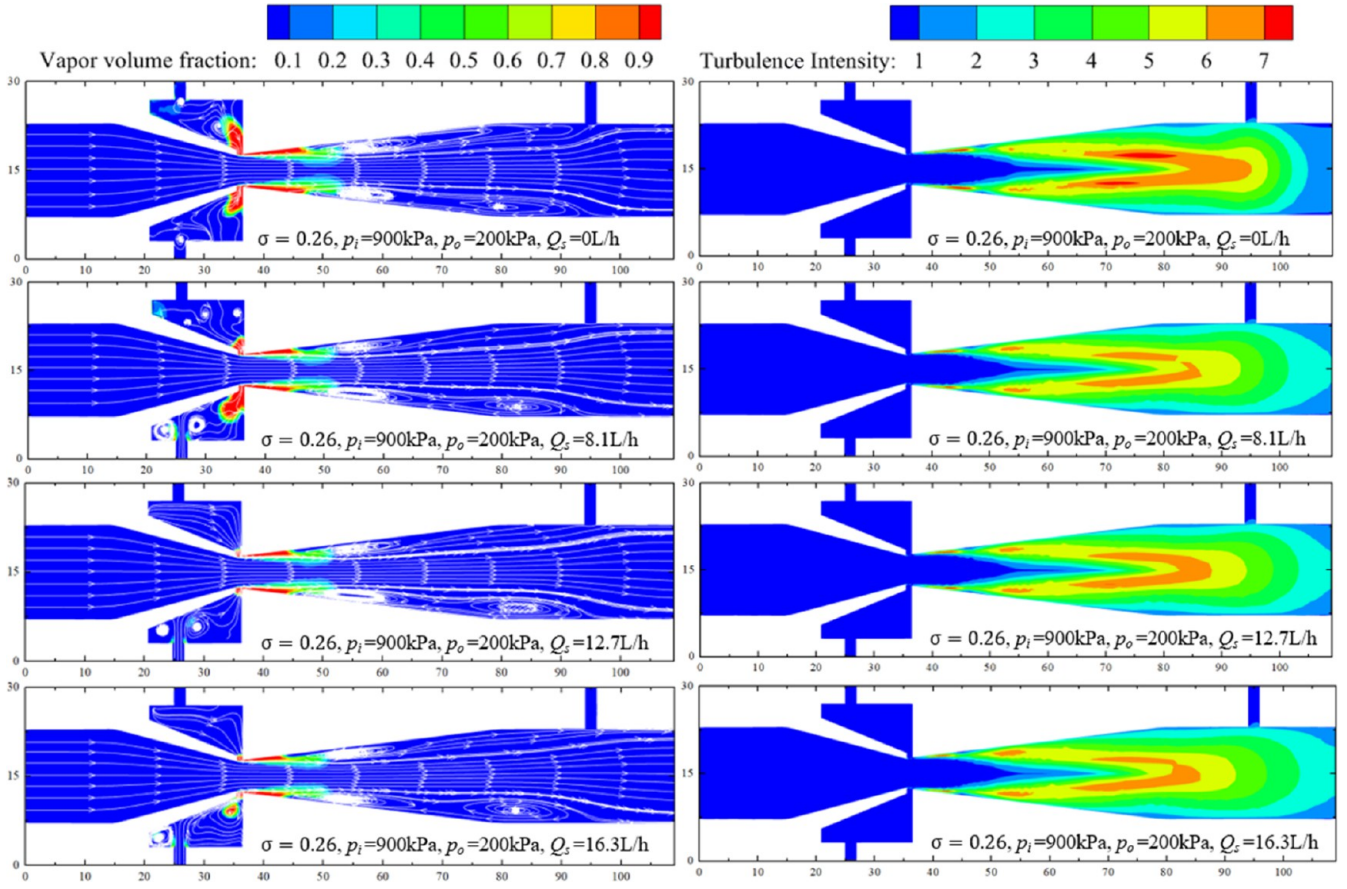

Figure 25. Distribution of vapor volume fraction and turbulence intensity in the cross-section when Z = 0 mm under different secondary flow rates Q_s.

the secondary flow rate Q_s. However, when Q_s = 16.3 L/h, this rule is invalid. The results indicate that the pressure loss law of cross-section a−b (as described in the first paragraph of Section 4.3) has a greater impact on the pressure loss of the jet pump. Therefore, the model needs to be improved to obtain accurate detection of the pressure on cross-sections b−b and c−c.

As shown in Figure 20, when Q_s = 0, for a constant cavitation number σ, the pressure losses of cross-sections a−b, b−c, c−d, and a−d increase as the inlet pressure increases. However, the slopes of the fitting curves of c−d and a−d pressure losses increase with the increases of the inlet pressure p_i (Figure 20c,d). This means that the greater the inlet pressure p_i is, the wider the range of pressure loss between cross-sections c−d and a−d is.

4.4. Numerical Simulation Analysis on the Cavitation Energy Loss. According to Figure 21, when the cavitation number σ = 0.26, the cavitation bubbles cover the confluence of the primary and secondary flows of cross-section b−c and the entrance near the wall of cross-section c−d. However, the turbulence intensity nephograms show that only cross-section c−d is covered. With the increase in the cavitation number σ, cavitation bubbles finally disappear at the confluence of primary and secondary flows in cross-section c−d. The area covered by turbulence intensity also shrinks gradually. When σ = 0.52, the cavitation intensities and turbulence intensities of cross-sections b−c and c−d decrease, and the coverage area also shrinks notably. When σ = 0.97, the turbulence intensity cloud appears at the confluence of the primary flow and the secondary flow of cross-section c−d. The above analysis suggests that when the inlet pressure p_i and secondary flow rate Q_s are constant, an increase in the cavitation number σ reduces the maximum cavitation intensity of cross-sections b−c and c−d, the position for cavitation bubbles collapses, and the generated turbulence also moves upstream, thus increasing the maximum turbulence intensity of cross-section b−c.

As shown in the colored dots in Figure 24b, the position on the X-axis for the maximum turbulence intensity first retreats upstream and then extends downstream with the increase in the cavitation number. This is because the regression of the turbulence intensity at the entrance of the diffusion tube results in the strong turbulence getting closer to the X-axis, which has a great influence on the turbulence intensity on the X-axis (the red arrows in Figure 21). When σ > 0.52 (Figure 21), the maximum turbulence intensity near the X-axis of the diffuser inlet begins to decrease, which leads to the extension of the maximum turbulence intensity on the X-axis to the downstream of the primary flow. Moreover, as shown by the streamlines in Figure 21, the vortices often appear downstream of the vapor volume fraction coverage. With the increase in the cavitation number σ, the vortices also move upstream along the vapor−liquid interface. This results from the turbulent flow near the wall caused by the collapse of a large number of bubbles at the confluence of the vapor−liquid surface.

It is crucial to choose a threshold for iso-surface visualization in the Q-criterion, so the criteria for choosing appropriate thresholds in this study are as follows: (1) the main structures

https://doi.org/10.1021/acsomega.1c06895
ACS Omega 2022, 7, 12661−12679

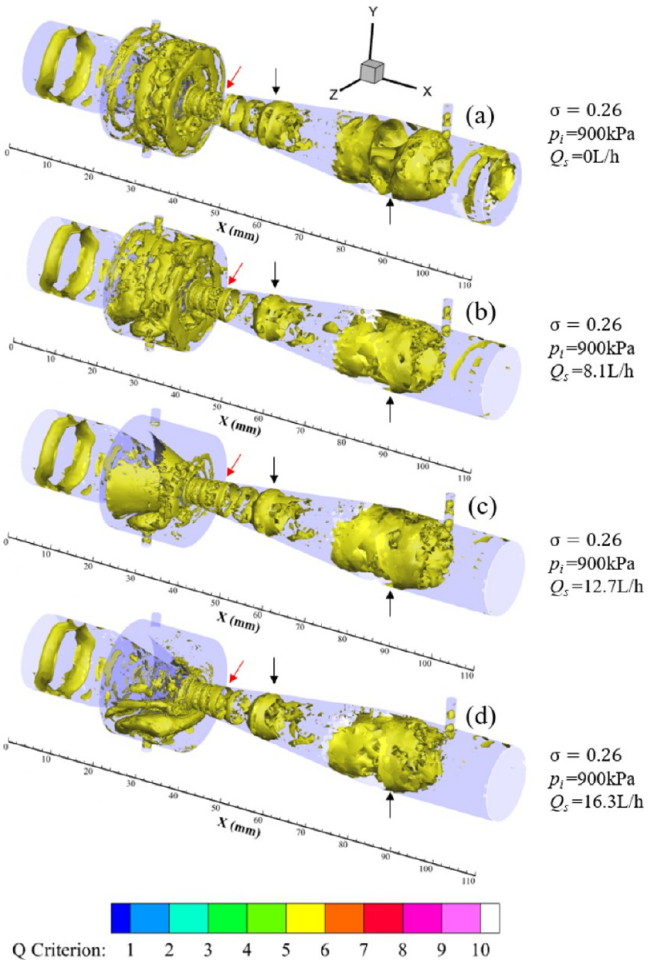

Figure 26. Variation of vortices with Q_s when σ = 0.26. (a) Q_s = 0 L/h, (b) Q_s = 8.1 L/h, (a) Q_s = 12.7 L/h, and (a) Q_s = 16.3 L/h.

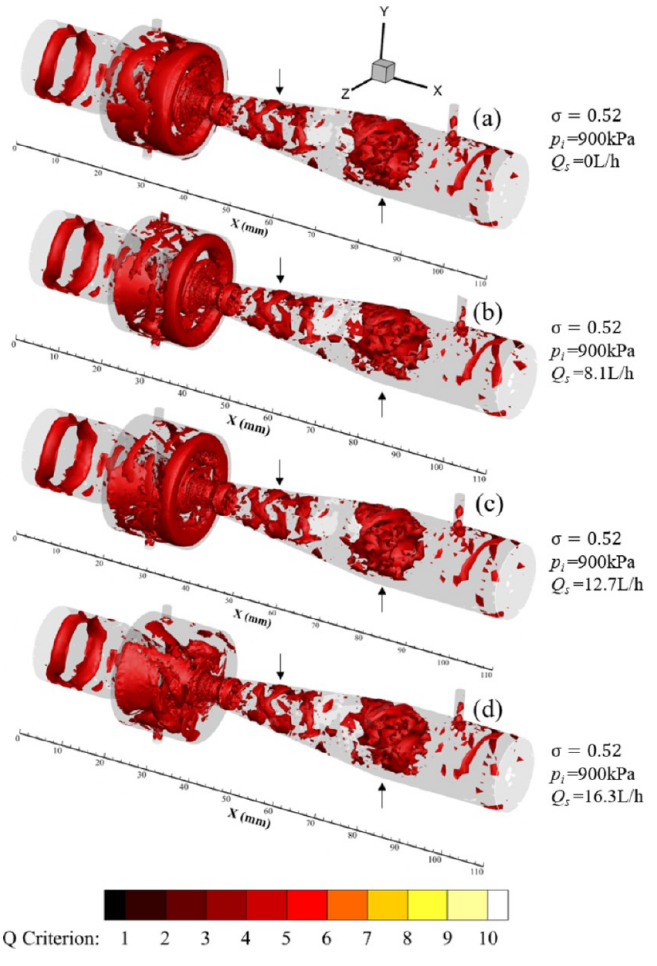

Figure 27. Variation of vortices with Q_s when σ = 0.52. (a) Q_s = 0 L/h, (b) Q_s = 8.1 L/h, (a) Q_s = 12.7 L/h, and (a) Q_s = 16.3 L/h.

should be clear and (2) small vortices should not be lost in large quantities.

As shown in Figures 22 and 23, in the cavitation state, vortices mainly appear in cross-sections b−c and c−d. The vortices in cross-section c−d appear at the inlet and the end of the diffuser. The vortex at the inlet of the diffuser is attached to the inner wall of the jet pump, while the vortex at the tail end nearly covers the entire radial section of the diffuser. According to the red arrows in Figures 22 and 23, although an increase in the cavitation number exerts a great influence on the vortex intensity in the cavitation cavity, the vortex shape of the mixing part of the primary flow and secondary flow remains unchanged, indicating that the vortex intensity in this part does not vary. As shown by the black arrows in Figures 22 and 23, as the cavitation number σ increases, the vortices change from spherical ones to fragmented ones. This indicates that as the cavitation number σ increases, the vortex intensities at the inlet and tail end of the diffusion tube decrease significantly, yet the vortices in cross-sections a−b and b−c vary slightly.

As shown in Figure 24a−c, the maximum vapor volume fraction and turbulence intensity on the X-axis correspond to the lowest temperature of the fluid in the corresponding part. This shows that the generation of cavitation bubbles absorbs energy from the surrounding liquid, while the collapse of bubbles releases energy. When σ = 0.26, Q_s = 8.1 L/h, and X > 55 mm, the bubbles collapse and disappear, and the turbulence intensity begins to increase. As shown in Figure 24c, the temperature variation begins to slow down. When the turbulence intensity reaches the maximum, the temperature decreases to the lowest value. This indicates that an increase in turbulence intensity consumes the liquid energy and reduces its temperature.

As shown in Figure 25, when the cavitation number σ is a constant value, the coverage range of cavitation bubbles in cross-section c−d shrinks with the increase in Q_s. Also, the vortex in the streamline chart also moves upstream. With the increase in the secondary flow rate Q_s, the area covered by the turbulence intensity cloud expands, but the area covered by the maximum turbulence intensity shrinks obviously. This indicates that the secondary flow rate Q_s has a certain inhibitory effect on the maximum cavitation intensity and turbulence intensity but can expand the turbulent coverage.

According to the positions indicated by the red arrows in Figure 26, when Q_s = 0 L/h, there is a clear gap in the annular vortices. When Q_s = 8.1 and 12.7 L/h, filamentous connections appear in the annular vortices. When Q_s = 16.3 L/h, the interval disappears. As indicated by the black arrows in Figures 26 and 27, the vortex intensity in the diffusion tube varies insignificantly with the increase in the secondary flow rate Q_s. The results show that as the secondary flow rate Q_s increases, the strong vortices in the cavitation cavity change into weak ones, the vortex at the entrance of the diffusion tube increases obviously, and other parts change slightly.

https://doi.org/10.1021/acsomega.1c06895
ACS Omega 2022, 7, 12661−12679

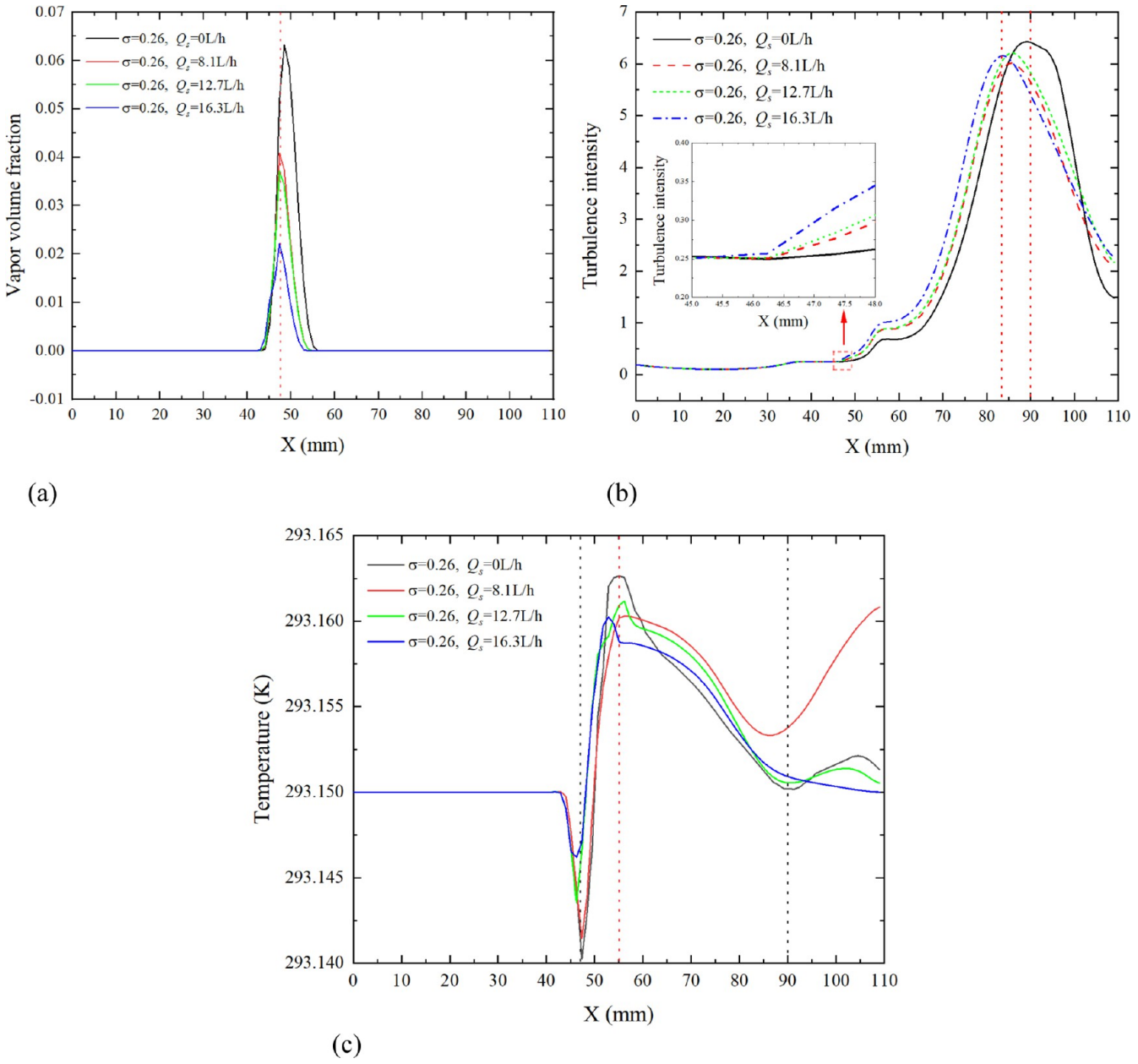

Figure 28. Distribution of vapor volume fraction, turbulence intensity, and temperature on the *X*-axis under different secondary flow rates Q_s. (a) Vapor volume fraction distribution on the *X*-axis. (b) Turbulence intensity distribution on the *X*-axis. (c) Temperature distribution on the *X*-axis (Figure 3).

As shown in Figures 25 and 28a, when σ and p_i are constant, the maximum cavitation intensity on the *X*-axis decreases with the increase in Q_s. As shown in Figure 28b, the maximum turbulence intensity also decreases with the increase in the secondary flow rate Q_s generally. When 80 mm > *X* > 45 mm, the turbulence intensity increases with the increase in Q_s. As shown in Figure 28a,c, when *X* = 43 mm, the temperature begins to fall, yet the vapor volume fraction begins to increase. When *X* = 55 mm, the vapor volume fraction is 0, and the temperature reaches the maximum. Compared with the vapor volume fraction nephograms in Figure 25, it can be seen that the lowest temperature on the *X*-axis appears on the red and blue interfaces of the cavitation nephogram, where the bubble density is the highest. The highest temperature occurs at the strong turbulence at the end of the cavitation cloud (where bubbles collapse). The positions of the black dashed line on the *X*-axis in Figure 28c are consistent with the positions corresponding to the red dashed lines in Figure 28a,b.

The relationship among the cross-section temperature, vapor volume fraction, and turbulence intensity of the diffusion tube are displayed intuitively in Figure 29. When *X* = 48.44 mm, the vapor volume fraction is the largest, the fluid temperature is the lowest, and the turbulence intensity is not 0. Therefore, the cross-section when *X* = 48.44 mm was selected for analysis.

As shown in Figure 29, the high temperature area of the cross-section fluid domain corresponds to the low value area of the vapor volume fraction and turbulence intensity, while the low temperature area corresponds to the high value area. This suggests that temperature is negatively correlated with vapor volume fraction and turbulence intensity. As shown in Figure 29a,b, when Q_s = 0, the temperature gradient on the cross-section is the highest; when Q_s = 8.1 L/h, the temperature

https://doi.org/10.1021/acsomega.1c06895
ACS Omega 2022, 7, 12661−12679

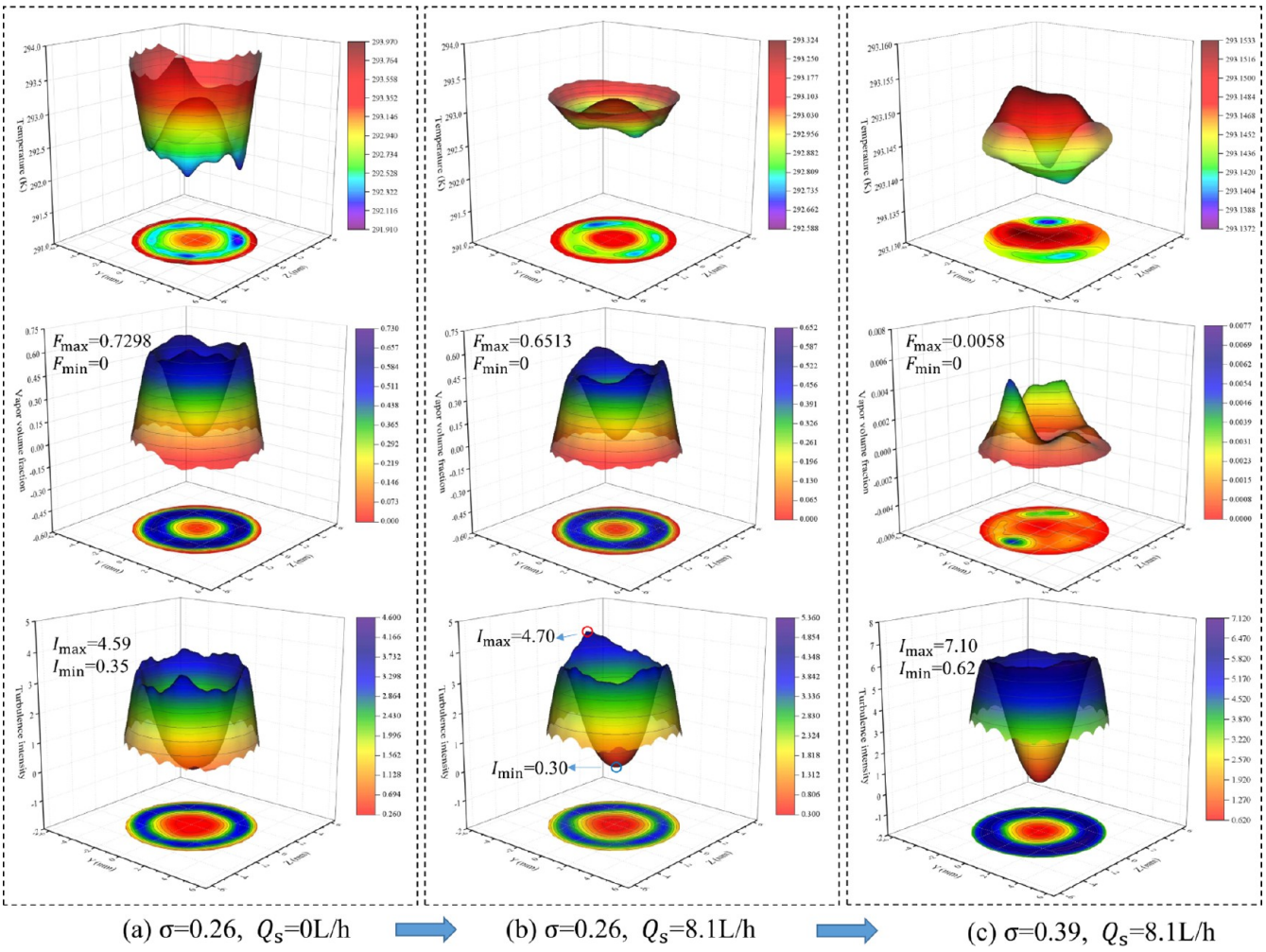

Figure 29. Variations of temperature, vapor volume fraction, and turbulence intensity with σ and Q_s in the cross-section when X = 48.44 mm.

gradient and vapor volume fraction gradient decrease significantly, yet the gradient range of turbulence intensity increases. When Y = −2.59 mm and Z = 2.01 mm, I_{max} = 4.70. This is because an increase in Q_s converts the heat energy of the cavitation bubbles into the kinetic energy of the secondary flow, thus reducing the vapor volume fraction of the cavitation bubbles. The main influence area is in the negative direction of the Y-axis. When σ increases from 0.26 to 0.39, the temperature gradient and vapor volume fraction gradient decrease obviously, while the high temperature coverage area and the turbulence intensity gradient surge. This is because an increase in p_o makes the coverage range of the cavitation bubbles regress in the direction of the incoming flow (i.e., the negative pressure area begins to shrink), and a large number of cavitation bubbles collapse at the cross-section when X = 48.44 mm. Part of the heat generated by bubble collapse is converted into fluid heat energy, resulting in a significant expansion of the high temperature area, and part of the heat is converted into kinetic energy, resulting in an increase in the turbulence intensity.

5. CONCLUSIONS

In this study, the head loss and pressure loss laws of the nozzle zone (a−b), mixing zone (b−c), and diffusion zone (c−d) of a jet pump were studied by changing the values of σ, Q_s, p_i, and p_o. The experimental results were verified using computational fluid dynamics (CFD). The main conclusions are as follows:

(1) With the increase of the pressure ratio, the jet pump has an obvious cavitation transitional stage. At this stage, as the pressure ratio increases slowly, the flow ratio begins to decrease. Increasing the secondary flow rate Q_s can effectively weaken the variations of the secondary flow rate Q_s and suction negative pressure p_s with the increase in the outlet pressure p_o.

(2) The variation laws of head loss in different sections of the jet pump with σ, Q_s, p_i, and p_o are as follows: when $\sigma < \sigma_{cr}$ and p_i and Q_s are constant values, H_{a-b} and H_{b-c} correspond to constant values, while H_{c-d} and H_{a-d} decrease linearly with the increase in the cavitation number. When p_i and σ are constant values ($\sigma < \sigma_{cr}$), H_{b-c} decreases, yet H_{c-d} increases with the increase in Q_s. When Q_s = 0, and σ remains at a constant value ($\sigma < \sigma_{cr}$), H_{a-b}, H_{b-c}, H_{c-d}, and H_{a-d} increase with the increase in p_i, and the variations of H_{c-d} and H_{a-d} intensify with the increase in p_i.

(3) When the cavitation number σ is at a constant value, as Q_s increases, the vortex at the entrance of the diffusion tube surges obviously, and the strong vortices in the cavitation cavity change into weak ones. The coverage area of the cavitation bubble cloud and maximum turbulence intensity in the diffusion tube shrinks, while

https://doi.org/10.1021/acsomega.1c06895
ACS Omega 2022, 7, 12661−12679

the coverage area of the turbulence intensity cloud expands. The results indicate that the secondary flow rate Q_s has different effects on the cavitation intensity and turbulence intensity in different parts of the jet pump.

(4) In the cavitation state ($\sigma < \sigma_{cr}$), the main factors affecting head loss are the cavitation intensity and turbulence intensity of the jet pump. On the cross-section in the jet direction (X = 48.44 mm), the vapor volume fraction and turbulence intensity are negatively correlated with the fluid temperature. The variations of Q_s and σ significantly influence the vapor volume fraction gradient and turbulence intensity gradient, which is essentially the result of energy conversion.

AUTHOR INFORMATION

Corresponding Author

Deming Wang − *Key Laboratory of Gas and Fire Control for Coal Mines, School of Safety Engineering, China University of Mining and Technology, Xuzhou 221116, China;* orcid.org/0000-0002-4324-9397; Email: dmwcumt@outlook.com

Authors

Jian Gan − *Key Laboratory of Gas and Fire Control for Coal Mines, School of Safety Engineering, China University of Mining and Technology, Xuzhou 221116, China*

Yanan Wang − *Key Laboratory of Gas and Fire Control for Coal Mines, School of Safety Engineering, China University of Mining and Technology, Xuzhou 221116, China*

Kang Zhang − *Key Laboratory of Gas and Fire Control for Coal Mines, School of Safety Engineering, China University of Mining and Technology, Xuzhou 221116, China*

Complete contact information is available at: https://pubs.acs.org/10.1021/acsomega.1c06895

Author Contributions

J.G. and Y.W. contributed equally to this work. J.G.: investigation, data curation, and writing—original draft. Y.W.: visualization and investigation. D.W.: conceptualization and methodology. K.Z.: investigation−review and editing.

Notes

The authors declare no competing financial interest.

ACKNOWLEDGMENTS

This project was supported by the Key Program of the National Natural Science Foundation of China (grant no. 52130411) and the National Natural Science Foundation of China (grant no. 51974299).

NOMENCLATURE

p_i, static pressure at the inlet (kPa)
p_s, static pressure at the suction tube inlet (kPa)
p_o, static pressure at the outlet (kPa)
Q_s, suction volume flow rate (L/h)
Q_o, outlet volume flow rate (L/s)
Q_p, primary volume flow rate (L/s)
v_l, velocity of the fluid (m/s)
$p_{i,abs}$, absolute pressure value of the inlet (kPa)
$p_{o,abs}$, absolute pressure value of the outlet (kPa)
H_{a-b}, head loss between cross-sections a−a and b−b (m)
H_{b-c}, head loss between cross-sections b−b and c−c (m)
H_{c-d}, head loss between cross-sections c−c and d−d (m)
H_{a-d}, head loss between cross-sections a−a and d−d (m)
H_{a-a}, water head on cross-section a−a (m)
H_{b-b}, water head on cross-section b−b (m)
H_{c-c}, water head on cross-section c−c (m)
H_{d-d}, water head on cross-section d−d (m)
p_a, mass average static pressure on cross-section a−a (kPa)
p_b, mass average static pressure on cross-section b−b (kPa)
p_c, mass average static pressure on cross-section c−c (kPa)
p_d, mass average static pressure on cross-section d−d (kPa)
v_a, average velocity of the water outlet or inlet on cross-section a−a (m/s)
v_b, average velocity of the water outlet or inlet on cross-section b−b (m/s)
v_c, average velocity of the water outlet or inlet on cross-section c−c (m/s)
v_d, average velocity of the water outlet or inlet on cross-section d−d (m/s)
ρ, density of the primary flow (kg/m^3)
U, speed in the the directions of x
V, speed in the the directions of y
W, speed in the the directions of z

DIMENSIONLESS SYMBOLS

σ cavitation number
σ_{in} incipient cavitation number
σ_{cr} critical cavitation number
v characteristic velocity
L characteristic length of the flow field
h_{cr} critical pressure ratio
α_1 kinetic energy correction coefficient on cross-section a−a
α_2 kinetic energy correction coefficient on Cross-section b−b
R_e Reynolds number
I turbulence intensity
h pressure ratio (the ratio of the absolute outlet pressure to absolute inlet pressure)
h_t transition pressure ratio
q_r flow ratio (the ratio of the suction flow rate to primary flow rate)
μ dynamic viscosity coefficient
F vapor volume fraction

REFERENCES

(1) Wang, H.; Wang, D.; Lu, X.; Gao, Q.; Ren, W.; Zhang, Y. Experimental investigations on the performance of a new design of foaming agent adding device used for dust control in underground coal mines. *J. Loss Prev. Process Ind.* **2012**, *25*, 1075−1084.

(2) Raut-Jadhav, S.; Badve, M. P.; Pinjari, D. V.; Saini, D. R.; Sonawane, S. H.; Pandit, A. B. Treatment of the pesticide industry effluent using hydrodynamic cavitation and its combination with process intensifying additives (H 2 O 2 and ozone). *Chem. Eng. J.* **2016**, *295*, 326−335.

(3) Long, X.; Zhang, J.; Wang, Q.; Xiao, L.; Xu, M.; Lyu, Q.; Ji, B. Experimental investigation on the performance of jet pump cavitation reactor at different area ratios. *Exp. Therm. Fluid Sci.* **2016**, *78*, 309−321.

(4) Lu, X.; Wang, D.; Shen, W.; Cao, K. A New Design of Double-Stage Parallel Adding Equipment Used for Dust Suppression in Underground Coal Mines. *Arabian J. Sci. Eng.* **2014**, *39*, 8319−8330.

(5) Hernandez-Alvarado, F.; Kalaga, D. V.; Turney, D.; Banerjee, S.; Joshi, J. B.; Kawaji, M. Void fraction, bubble size and interfacial area measurements in co-current downflow bubble column reactor with microbubble dispersion. *Chem. Eng. Sci.* **2017**, *168*, 403−413.

(6) Liu, K.; Lu, H.; Guo, X.; Sun, X.; Tao, S.; Gong, X. Experimental study on flow characteristics and pressure drop of gas-coal mixture through venturi. *Powder Technol.* **2014**, *268*, 401−411.
(7) Lima, D. D.; Lima Neto, I. E. Air entrainment and pressure drop in low-cost ejectors. *Ann. Acad. Bras. Cienc.* **2020**, *92*, No. e20191444.
(8) Zhu, X.; Wang, D.; Xu, C.; Zhu, Y.; Zhou, W.; He, F. Structure influence on jet pump operating limits. *Chem. Eng. Sci.* **2018**, *192*, 143−160.
(9) Lu, X.-x.; Wang, D.-m.; Zhu, C.-b.; Shen, W.; Zhong, X.-x.; Xu, C.-h. A new adding method of foaming agent used for foam dust suppression in underground coal mines. *J. Cent. South Univ.* **2015**, *22*, 3116−3122.
(10) Gao, T. Pipe Roughness Estimation in Water Distribution Networks Using Head Loss Adjustment. *J. Water Resour. Plann. Manag.* **2017**, *143*, 4017007.
(11) Yang, X. C.; Cao, Y. G. Effects of head loss, surface tension, viscosity and density ratio on the Kelvin-Helmholtz instability in different types of pipelines. *Phys. D* **2021**, *424*, 132950.
(12) Chen, Y.; Li, Y.; Zhou, X.; Xie, Y. A multi-level assessment and correction method for Venturi tube flow measurements. *Nucl. Eng. Des.* **2021**, *379*, 111262.
(13) Jiang, C.; Gong, Z. Effect of Deflectors on the Flow Characteristics of a Square Pipe with a 90° Bend. *J. Shanghai Jiaot. Univ.* **2021**, *26*, 163−169.
(14) Royne, A.; Dey, C. J. Effect of nozzle geometry on pressure drop and heat transfer in submerged jet arrays. *Int. J. Heat Mass Transfer* **2006**, *49*, 800−804.
(15) Brignoni, L. A.; Garimella, S. V. Effects of nozzle-inlet chamfering on pressure drop and heat transfer in confined air jet impingement. *Int. J. Heat Mass Transfer* **2000**, *43*, 1133−1139.
(16) McNeil, D. A.; Stuart, A. D. Vertically upward two-phase flow with a highly viscous liquid-phase in a nozzle and orifice plate. *Int. J. Heat Fluid Flow* **2004**, *25*, 58−73.
(17) Zhu, X.; Wang, D.; Wang, H.; Zhu, Y.; Xu, C. A cavitating device for mini quantitative liquid addition. *Flow Meas. Instrum.* **2017**, *57*, 87−93.
(18) Lu, X.; Wang, D.; Shen, W.; Zhu, C.; Chen, M. Experimental investigation on the performance of improving jet pump cavitation with air suction. *Int. J. Heat Mass Transfer* **2015**, *88*, 379−387.
(19) Bhusare, V. H.; Kalaga, D. V.; Dhiman, M. K.; Joshi, J. B.; Roy, S. Mixing in a co-current upflow bubble column reactors with and without internals. *Can. J. Chem. Eng.* **2018**, *96*, 1957−1971.
(20) Bhusare, V. H.; Dhiman, M. K.; Kalaga, D. V.; Roy, S.; Joshi, J. B. CFD simulations of a bubble column with and without internals by using OpenFOAM. *Chem. Eng. J.* **2017**, *317*, 157−174.
(21) Long, X. P.; Zeng, Q. L.; Yang, X. L.; Xiao, L. Structure optimization of an annular jet pump using design of experiment method and CFD. *IOP Conf. Ser. Earth Environ. Sci.* **2012**, *15*, 052020.
(22) Salim, S.M.; Cheah, S.. Wall y+ Strategy for Dealing with Wall-bounded Turbulent Flows. *Proceedings of the International Multi-Conference of Engineers and Computer Scientists*; IMECS, 2009; Vol. 2. ISBN: 978-988-17012-7-5.
(23) Ginting, B. M. Central-upwind scheme for 2D turbulent shallow flows using high-resolution meshes with scalable wall functions. *Comput. Fluid* **2019**, *179*, 394−421.
(24) Ulas, A. Passive flow control in liquid-propellant rocket engines with cavitating venturi. *Flow Meas. Instrum.* **2006**, *17*, 93−97.
(25) Abdulaziz, A. M. Performance and image analysis of a cavitating process in a small type venturi. *Exp. Therm. Fluid Sci.* **2014**, *53*, 40−48.
(26) Liu, J.-m.; Wang, Y.-q.; Gao, Y.-s.; Liu, C. Galilean invariance of Omega vortex identification method. *J. Hydrodyn.* **2019**, *31*, 249−255.
(27) Liu, C.; Wang, Y.; Yang, Y.; Duan, Z. New omega vortex identification method. *Sci. China Phys. Mech. Astron.* **2016**, *59*, 684711.

https://doi.org/10.1021/acsomega.1c06895
ACS Omega 2022, 7, 12661−12679